Catalysis Today 144 (2009) 235–250

Contents lists available at ScienceDirect

Catalysis Today

journal homepage: www.elsevier.com/locate/cattod

Deep desulphurization of diesel fuels on bifunctional monolithic nanostructured Pt-zeolite catalysts

Zinfer R. Ismagilov [a], Svetlana A. Yashnik [a,*], Anatolii N. Startsev [a], Andrei I. Boronin [a], Andrei I. Stadnichenko [a], Vladimir V. Kriventsov [a], Slavik Kasztelan [b], Denis Guillaume [b], Michiel Makkee [c], Jacob A. Moulijn [c]

[a] Boreskov Institute of Catalysis, Novosibirsk, Russia
[b] Institut Francais du Petrole, IFP-Lyon, France
[c] Delft University of Technology, Delft, The Netherlands

A R T I C L E I N F O

Article history:
Available online 23 February 2009

Keywords:
Pt-zeolite
Hydrodesulphurization
Ultra-deep desulphurization
Hydrogenation
Diesel fuel

A B S T R A C T

The preparation of Pt-zeolite catalysts, including choice of the noble metal precursor and loading (1.0–1.8 wt.%), was optimized for maximizing the catalytic activity in thiophene hydrodesulphurization (HDS) and benzene hydrogenation (HYD). According to data obtained by HRTEM, XPS, EXAFS and FTIR spectroscopy of adsorbed CO, the catalysts contained finely dispersed Pt nanoparticles (2–5 nm) located on montmorillonite and zeolite surfaces as: Pt^0 (main, $\nu_{CO} = 2070–2095\ cm^{-1}$), $Pt^{\delta+}$ ($\nu_{CO} = 2128\ cm^{-1}$) and Pt^{2+} ($\nu_{CO} = 2149–2155\ cm^{-1}$). It was shown that the state of Pt depended on the Si/Al zeolite ratio, montmorillonite presence and Pt precursor. The use of H_2PtCl_6 as the precursor (impregnation) promoted stabilization of an oxidized Pt state, most likely $Pt(OH)_xCl_y$. When $Pt(NH_3)_4Cl_2$ (ion-exchange) was used, the Pt^0 and hydroxo- or oxy-complexes $Pt(OH)_6{}^{2-}$ or PtO_2 were formed. The addition of the Ca-montmorillonite favoured stabilization of $Pt^{+\delta}$. The Cl^- ions inhibit reduction of oxidized Pt state to Pt particles. The Pt-zeolite catalyst demonstrated high efficiency in ultra-deep desulphurization of DLCO. The good catalyst performance in hydrogenation activity and sulphur resistance can be explained by the favourable pore space architecture and the location and the state of the Pt clusters. The bimodal texture of the developed zeolite substrates allows realizing a concept for design of sulphur-resistant noble metal hydrotreating catalyst proposed by Song [C. Song, Shape-Selective Catalysis, Chemicals Synthesis and Hydrocarbon Processing (ACS Symposium Series 738), Washington, 1999, p. 381; Chemtech 29(3) (1999) 26].

1. Introduction

In the last decade, requirements to the concentration of harmful substances in the exhaust gases of gasoline and diesel engines keep getting much stricter [1]. This tendency led to stricter requirements to the quality of motor fuel. According to the Directive of the European Union, diesel fuel in Europe should not contain more than 50 ppm sulphur (ultra-low-sulphur-diesel–ULSD, EURO-IV) starting from 2005, no more than 10 ppm sulphur (near-zero-sulphur-diesel–NZSD, EURO-V) starting from 2010, and no more than 10 vol.% of aromatic substances [2]. According to the US regulations, the sulphur concentration in diesel fuel should not exceed 15 ppm starting from June 2006 [3]. All diesel fuel produced in Russia should conform to the EURO-IV standards starting from 2010.

The industrial hydrodesulphurization catalysts $CoMo/Al_2O_3$ and $NiMo/Al_2O_3$ decreased typically the sulphur concentration in diesel fuel to 350–500 ppm [4,5]. The new present-day catalysts such as TK558-Brim, TK559-Brim and TK576-Brim provide a decrease of sulphur content to 50 ppm [6]. To purify diesel fuel to 50 ppm S or less one has to remove the least-reactive sulphur-containing-alkyl-substituted dibenzothiophenes [7–10] while maintaining the other diesel fuel requirements such as the cetane number, density, polynuclear aromatics contents and 95% distillation point [2,3]. The conventional supported $CoMo/Al_2O_3$ and $NiMo/Al_2O_3$ sulphide hydrodesulphurization catalysts cannot accomplish these tasks.

Usually crude oil contains a wide range of sulphur-containing compounds: mercaptans, sulphides, thiophenes, benzothiophenes and their alkyl-substituted derivatives. The reactivity of organosulphur compounds depends on their structure and local environment of the sulphur atom [8,11]. Low-boiling oil fractions

---

* Corresponding author at: Boreskov Institute of Catalysis, Pr. Akad. Lavrentieva, 5 Novosibirsk 630090, Russia.
E-mail address: yashnik@catalysis.ru (S.A. Yashnik).

0920-5861/$ – see front matter © 2009 Elsevier B.V. All rights reserved.
doi:10.1016/j.cattod.2009.01.030

contain mainly aliphatic organosulphur compounds: mercaptans, sulphides and disulphides that are easily and completely removed in industrial hydrodesulphurization processes over $CoMo/Al_2O_3$ and $NiMo/Al_2O_3$ sulphide catalysts [11]. These substances can be easily eliminated by non-catalytic methods as well, e.g. by Merox process [11]. Meanwhile, organosulphur compounds containing the thiophene ring predominate in heavier oil fractions, such as diesel fraction, light and heavy gasoil [11]. It is more difficult to eliminate them by hydrodesulphurization compared to mercaptans and sulphides. The oil fractions such as bottom fluid catalytic cracking (FCC) naphtha, coker naphtha, FCC and coker diesel contain mostly alkylated benzothiophenes, dibenzothiophene and its derivates, as well as polynuclear organosulphur compounds [11], which have very low reactivity in hydrodesulphurization reactions.

Solution of the deep hydrodesulphurization problem requires either improvement of severity of industrial hydrodesulphurization processes (increase of the process temperature and pressure [10–13], decrease of the feed flow rate [10]) or development of new catalysts with high activity and selectivity [10–14]. However, more severe conditions of the HDS process are not always possible. For example, higher pressure leads to olefins saturation, and higher temperature results in increased coke formation and subsequent catalyst deactivation. When the fuel feed flow rate is considerably reduced, the catalyst lifetime is shortened. It is most desirable economically to increase the activity and selectivity of the catalysts. This is the reason why the interest of researchers to development of catalytic systems for hydrodesulphurization processes does not go down.

The main approaches to improvement of the catalysts for deep hydrodesulphurization can be tentatively divided into three groups:

(1) Development of new methods for deposition and activation of the active component in $Co(Ni)Mo(W)/Al_2O_3$ catalysts [6,13–18];
(2) Application of improved supports with optimal textural and acid–base properties, e.g. amorphous silicates, mixtures of silica, titania or zirconia with alumina, zeolites [13,14,19–24];
(3) Application of active complexes different from Co(Ni)MoS that have high hydrogenation activity, e.g. Pt, Pd [25–29], nitrides [30], carbides [30–32], phosphides [33,34].

Each of these three approaches for improvement of the catalyst increases the efficiency of the motor fuel desulphurization mostly by changing the reaction pathway from direct desulphurization (DDS) to preliminary conversion of alkyldibenzothiophenes to more reactive molecules by “benzene ring hydrogenation” (HYD), isomerization and dealkylation [10–14]. The catalytic activity in HYD reaction is mostly determined by the catalyst hydrogenation properties that can be increased by introduction of appropriate metals, such as Ni and W [4,15], Pt [25], Pd [27,29,35–38], and/or use of a suitable support [25–28]. The activity in other, non-HYD reactions, mostly depends on the acid–base properties of the support [10,12–14].

Today, catalysts based on Pt and Pd supported on various oxide supports [23,24,28,29] or zeolite-containing materials [25–27] are considered as candidates for second stage of two-stage deep hydrodesulphurization of motor fuels when the oil fraction is already mostly desulphurized on sulphide catalysts $CoMo/Al_2O_3$ and $NiMo/Al_2O_3$ [13,14,28]. PtPd/ASA catalysts are excellent for hydrodesulphurization of oil fractions with low concentrations of sulphur and aromatic substances [25,26]. However, supported PtPd/ASA catalysts are quickly deactivated by sulphur if its concentration in the fuel is high [11,26]. At high concentration of aromatic compounds Pt/ASA was found to be more active than PtPd/ASA [11,26]. Pd was found to be more active than Pt in hydrogenation reaction in the presence of sulphur components [29,35–38]. So, the introduction of a second metal, e.g. Pd to Pt, improves the catalytic activity in hydrogenation reaction in the presence of sulphur [39] and the catalytic performance in conversion of substituted dibenzothiophenes [40,41].

A new concept in design of hydrodesulphurization catalysts suggested by Song [10,42] makes it possible to improve the stability of noble metals to deactivation in hydrodesulphurization processes [10,11,25,27,42,43]. According to his concept, the catalyst must be bifunctional, have bimodal pore size distribution (e.g. zeolite) and two types of active sites [10,42]. The sites of the first type are located in large pores, accessible to large organosulphur molecules and sensitive to deactivation with sulphur. The sites of the second type are located in small pores (zeolite channels), inaccessible to organic molecules and stable to deactivation. Hydrogen easily penetrates into the small pores where it is dissociatively adsorbed. Then, it can move along the pore system and be used for regeneration of the deactivated sites of the first type. Such autoregeneration maintains the high activity even when the sulphur concentration on the oil fraction is high. However, this concept requires supports with suitable textural and surface properties to be developed.

The current study was devoted to rational design of nanostructured sulphur-tolerant Pt catalysts based on zeolite-monolithic materials and investigation of their activity in thiophene hydrogenolysis and benzene hydrogenation. These catalytic materials enable simultaneous ultra-deep desulphurization and dearomatization of petroleum feedstocks. FTIR spectroscopy of adsorbed CO molecules, electron microscopy (SEM and TEM), nitrogen adsorption, XPS and EXAFS were used for investigation of the state of Pt, morphology, textural and acid properties of the zeolite materials and catalysts. These data make it possible to arrive at fundamental understanding of relationships between their structure and catalytic performance.

2. Experimental

2.1. Catalyst preparation

The honeycomb zeolite-containing monoliths were prepared by extrusion according to the technique described in [44]. The extrusion masses were prepared by blending powdered experimental-industrial H-ZSM-5 zeolites (distinguished by the Si/Al atomic ratio) with a Ca-montmorillonite sol (Tagan’skoe deposit, Kazakhstan). The zeolite-containing monoliths were calcined at 600 °C for 4 h. The zeolite and Ca-montmorillonite loadings in the calcined monoliths were 65 wt.% and 35 wt.%, respectively. The physicochemical properties of the zeolite-containing materials are presented in Table 1.

Pt was introduced in the honeycomb zeolite-containing monolith by incipient wetness impregnation or by ion-exchange. For incipient wetness impregnation the zeolite-monolith was immersed in aqueous solutions of hexachloroplatinum acid, H_2PtCl_6, or tetraammineplatinum chloride, $Pt(NH_3)_4Cl_2$, with specified concentration for 15 min. Then, the monoliths were taken from the solutions, and solution excess was removed by compressed air flow.

For ion-exchange the zeolite-monolith was plunged into aqueous solutions of $Pt(NH_3)_4Cl_2$ with 2.5 mg Pt ml^{-1} concentration and kept for 2 days. Then, the zeolite-monolith was taken from the solution and washed with water, and excess of solution and water was removed by compressed air flow.

After the impregnation or ion-exchange procedure the monoliths were dried at 110 °C and calcined at 400 °C for 4 h. The Pt loadings were 0.8–1.9 wt.%. The physicochemical properties of the Pt-zeolite catalysts are presented in Table 2.

Table 1
Textural and physicochemical characteristics of monoliths prepared by extrusion of the oxide powder with montmorillonite sol.

Monolith	Oxide component	Pore structure[a]			S_{BET} ($m^2 g^{-1}$)	$S_{external}$ ($m^2 g^{-1}$)	Mechanical strength on generatrix (kg/cm^2)
		V_{Σ} ($cm^3 g^{-1}$)	V_{micro} ($cm^3 g^{-1}$)	D_{av} (nm)			
ZM-17	H-ZSM-5-17	0.28	0.08	4.5	265	89	10
ZM-30	H-ZSM-5-30	0.26	0.08	4.5	290	100	19
ZM-45	H-ZSM-5-45	0.36	0.07	4.7	250	98	21
YM	Na-Y	0.28	0.2	2.0	460	28	7
SiM	SiO_2	0.63	–	15.5	162	157	48
AlM	Al_2O_3	0.30	–	9.3	129	125	32
ZA[b]	H-ZSM-5-45	0.33	0.07	5.0	300	100	4
Z[c]	H-ZSM-5-45	0.25	0.095	–	127	346	–
M[d]	Montmorillonite	0.036	0.0001	6.0	23	24	–

[a] N_2 adsorption technique: V_{Σ}—total pore volume of pores between 1 and 300 nm, V_{micro}—micropore volume, D_{av}—BET average pore diameter, S_{BET}—BET surface area, $S_{external}$—surface area of crystallites.
[b] Prepared with Al hydroxide (as a binder).
[c] Powder of H-ZSM-5-45 calcined at 600 °C.
[d] Powder of Ca-montmorillonite calcined at 600 °C.

For comparison the catalysts based on H-ZSM-5 and Ca-montmorillonite powders were prepared under similar conditions. Their properties are also presented in Table 2.

The catalysts are designated in the text as follows: xPt(a)/Y-b, where x is the Pt loading (0.8–1.9 wt.%), a is the Pt precursor and preparation route (Cl—H_2PtCl_6, impregnation; A—$Pt(NH_3)_4Cl_2$, ion-exchange), Y is the support (Z—H-ZSM-5 zeolite powder; ZM—honeycomb monolith based on zeolite with montmorillonite, M—montmorillonite powder), and b is the zeolite Si/Al ratio (17, 30, and 45).

2.2. Physicochemical properties

The textural properties of the zeolite powders and the zeolite-containing monoliths-total pore volume (V_{Σ} $cm^3 g^{-1}$), volume of micropores (V_{micro}, $cm^3 g^{-1}$) and mesopores (V_{mezo}, $cm^3 g^{-1}$), specific surface area (S_{BET}, $m^2 g^{-1}$) and crystallite external surface area ($S_{external}$, $m^2 g^{-1}$)–were determined from the nitrogen adsorption isotherms. The nitrogen adsorption isotherms were measured at 77 K using ASAP-2400 instrument. The samples were degassed under vacuum at 570 K before the nitrogen adsorption. The micropore volumes and the crystallite external surface areas were calculated from the nitrogen desorption isotherm by the t-method. The data were processed according to the procedure described in [45]. Mercury porosimetry was used to study the macropore volume of the zeolite-containing monoliths.

The morphology of the zeolite-monoliths and Pt-zeolite catalysts was studied by scanning electron microscopy (SEM) and by transmission electron microscopy (TEM) using SEM-100-Y and JEM-100CX microscopes, respectively. For the SEM investigation the samples were pasted on the substrates and covered with a thin layer of gold to create a conducting layer. The accelerating voltage was 30 kV. For the TEM study the samples were dispersed in alcohol suspensions by means of an ultrasonic disperser and placed on copper grids with 3 mm diameter covered by a microperforated carbon film.

The Pt loading was determined by atomic absorption spectroscopy with inductively coupled plasma (AAS-ICP), employing a BLYRD analyzer. The catalyst was previously dissolved by heating in a mixture of concentrated hydrofluoric and sulphuric acids.

The acidic properties and the state of Pt in the Pt-zeolite catalysts were studied by FTIR spectroscopy, XPS and EXAFS.

The FTIR spectra were recorded using a BOMEM MB102 FTIR spectrometer. The adsorption of carbon monoxide was studied in a low-temperature spectroscopic cell equipped with CaF_2 glasses. Powdered samples were pressed into self-supported wafers of 15–25 mg cm^{-2} thickness. A catalyst pellet was placed into the spectroscopic cell, which was then connected to a vacuum adsorption apparatus. Prior to the adsorption measurements, the pellets were heated in air at 400 °C for 1 h and then pretreated under vacuum for 3 h at the same temperature to remove surface-adsorbed compounds and water. Then, the sample was cooled down to room temperature, and background spectra were recorded. Pure carbon monoxide was introduced into the cell at 1.3–2.6 mbar pressure. FTIR spectra were recorded at room temperature with spectral resolution of 2 cm^{-1} and accumulation

Table 2
HDS activity of Pt catalysts on substrates of different chemical composition.

Catalyst	Catalyst composition			Thiophene decomposition activity		
	Oxide component in substrate	Pt precursor	Pt loading (wt.%)	Initial/steady-state total conversion X_{C4H4S} (%)	Reaction rate W (mol C_4H_4S/mol Pt h)	Selectivity (%)
						C_4H_{10}/C_4H_8S
1Pt(Cl) ZM-17	H-ZSM-5-17	H_2PtCl_6	1.1	49/40	3500	52/48
1Pt(Cl)ZM-30	H-ZSM-5-30	H_2PtCl_6	1.0	38/33	2900	30/70
1Pt(Cl)ZM-45	H-ZSM-5-45	H_2PtCl_6	1.1	50/35	3100	40/60
2Pt(Cl)ZM-45	H-ZSM-5-45	H_2PtCl_6	1.8	48/45	2190	46/54
2Pt(A)ZM-45	H-ZSM-5-45	$Pt(NH_3)_4Cl_2$	1.6	52/40	1760	50/50
1Pt(Cl)YM	Na-Y	H_2PtCl_6	0.8	23/18	1045	51/49
1Pt(Cl)SiM	SiO_2	H_2PtCl_6	0.9	23/16	760	54/46
1Pt(Cl)AlM	Al_2O_3	H_2PtCl_6	0.9	33/22	1345	47/53
2Pt(Cl)ZA-45	H-ZSM-5-45	H_2PtCl_6	1.9	36/26	710	45/55
1Pt(Cl)Z-45	H-ZSM-5-45	H_2PtCl_6	1.22	58/46	3715	37/63
1Pt(A)Z-45	H-ZSM-5-45	$Pt(NH_3)_4Cl_2$	1.23	62/50	3090	47/53
1Pt(Cl)M	Montmorill	H_2PtCl_6	0.51	24/6	710	0/100
1Pt(A)M	Montmorill	$Pt(NH_3)_4Cl_2$	0.12	26/12	6700	26/74

of 64 scans. Then, the sample was cooled to −196 °C with liquid nitrogen, and FTIR spectra were recorded. This procedure gives information about the strength of Bronsted and Lewis acid sites of the support and the catalyst.

Spectral bands at 2070–2090 cm^{-1} and 2120–2150 cm^{-1} were used to identify Pt^0 particles and $Pt^{\delta+}/Pt^{2+}$ cations, respectively. The Pt^0 amount was calculated from the intensities of the corresponding spectral bands using BLB law: $A = 10^{-3} \cdot A_o \cdot C_s \cdot \rho$, where A is the observed integral absorbance, cm^{-1}; A_o is the integral extinction coefficient, cm/μmol; C_s is the adsorbate concentration, μmol/g; and ρ is the catalyst density, mg cm^{-2} [46]. The integral extinction coefficient equal to 11.7 cm/μmol [46] was used for the Pt^0 site.

XPS spectra were obtained by electron spectrometer VG ESCALAB HP (VG Scientific, Great Britain). Non-monochromatic Al K_α X-rays (1486.6 eV) were used as primary excitation. The Si 2p peak of silica from zeolite was selected as the internal standard, which value was accepted equal to 103.0 eV. Before spectroscopic measurements all samples were degassed in the preparation chamber up to pressure 10^{-7} mbar and subsequently moved in the analyzer chamber where the base vacuum was not above 10^{-9} mbar. The main background gases were CO, CO_2, and H_2O. The analysis of a platinum chemical state was carried out from analysis of core Pt4d- and Pt4f-levels. Difference spectra of the catalyst and the support samples were used except the Al2p line of alumina from the support, because of superposition of Al2p and Pt4f lines.

The EXAFS spectra of the Pt-L_3 edge for all the studied samples were obtained at the EXAFS Station of Siberian Synchrotron Radiation Center (SSRC, Novosibirsk). The storage ring VEPP-3 with the electron beam energy of 2 GeV and the average stored current of 80 mA has been used as the source of radiation. The X-ray energy was monitored with a channel cut Si(111) monochromator. All the spectra were recorded under transmission mode using ionization chambers filled with argon. For the EXAFS measurements, the samples were prepared as pellets with thickness varied to obtain ca. 0.5–1.0 jump at the absorption edges. The harmonic rejection was performed by a SiO_2 (quartz) mirror for all Pt-L_3 measurements. All EXAFS spectra were recorded with the steps of ca. 1.5 eV.

The EXAFS spectra were treated by the standard procedures [47]. The background was removed by extrapolating the pre-edge region onto the EXAFS region by Victoreen's polynomials. Three cubic splines were used to construct the smooth part of the absorption coefficient. The inflection point of the edge of the X-ray absorption spectrum was used as initial point ($k = 0$) of the EXAFS spectrum. The radial distribution function (RDF) of the atoms was calculated from the EXAFS spectra in $k^3\chi(k)$ as modulus of Fourier transform at the wave number intervals 3.5–13.5 $Å^{-1}$. Curve fitting procedure with EXCURV92 code [48] was employed to determine the distances (R) and effective coordination numbers (CN) in similar wave number intervals after preliminary Fourier filtering using the known XRD literature data for the bulk reference compounds. The values of Debye-Waller factors were fixed.

2.3. Catalytic tests in thiophene HDS and benzene HYD

The procedure of the catalytic experiments is presented in [49]. An experimental flow set-up with a fixed bed catalytic reactor was used for the catalyst testing. The thiophene hydrodesulphurization (HDS) reaction $C_4H_4S + 4H_2 \rightarrow H_2S + C_4H_{10}$ (C_4H_8) was studied in the kinetic region at 300 °C, hydrogen pressure 20 atm and weight-hourly space-velocity 0.7 h^{-1}. The hydrogen-to-thiophene volume ratio was equal to 500. The catalyst loading was 10 mg. The catalyst fraction with 0.25–0.5 mm size was used. A mixture of thiophene with cyclohexane was fed into the reactor with flowing hydrogen saturated by thiophene at 0 °C. The reaction mixture feed rate ($C_4H_4S + H_2$) was equal to 10 $cm^3\ s^{-1}$. The reaction products were analyzed using a LChM-8 chromatograph equipped with a flame-ionization detector and a packed column filled with tricresylphosphate supported on shimalite at the oven temperature of 60 °C. The chromatogram contained peaks corresponding to the C_4-products, tetrahydrothiophene and unreacted thiophene. Different C_4-components were not separated, only the total C_4 signal was considered for calculating the activity. The fractional conversion (α_{C4} and α_{C4H8S}) was calculated from the ratio of the concentrations of the C_4-products or tetrahydrothiophene to the sum of the concentrations of the products and thiophene. The total thiophene conversion was calculated as the sum of the fractional conversions α_{C4} and α_{C4H8S}.

The catalytic activity in the HDS reaction was evaluated as the rate (W_{HDS}, mol C_4H_4S/mol Pt^*h) of the pseudo-first-order thiophene HDS reaction. The rate was determined using the integral reactor equation: $W_{HDS} = -\ln(1-\alpha_{C4})^* V/W$, where α_{C4} is the the fractional conversion of C_4-products at the steady-state conditions ($\alpha_{C4} = C_4/(C_4 + C_4H_8S + C_4H_4S)$; C_4 and C_4H_8S are the concentrations of C_4-products and tetrahydrothiophene, respectively; C_4H_4S is the concentration of unreacted C_4H_4S; V is the C_4H_4S gas flow rate (mol C_4H_4S/h); and W is the Pt loading in the catalyst weight (mol Pt).

The benzene hydrogenation (HYD) reaction $C_6H_6 + 3H_2 \rightarrow C_6H_{12}$ was studied at 300 °C, pressure 20 atm, feed ($C_6H_6 + H_2$) flow rate 10 $cm^3\ s^{-1}$. Thiophene (1.2 wt.% based on the expectation of sulphur) was introduced in the reaction mixture ($C_6H_6 + H_2$) at the first stage of benzene HYD testing (I-stage). When the benzene conversion at the I-stage became stable, the thiophene feed was cut off (II-stage) while the benzene conversion was monitored. The catalyst loading was 10 mg. The catalyst fraction with 0.25–0.5 mm size was used.

The catalytic activity in HYD reaction was evaluated as the total conversion of benzene to cyclohexane (CH) and methylcyclopentane (MCP). The selectivities to CH and MCP were also measured.

2.4. Hydrodesulphurization and hydrogenation of DLCO

A "U23" pilot plant was used. This plant contains an isothermal fixed bed reactor operating in the up flow mode. The reactor with the catalyst volume of 40 ml has an interior diameter of 19 mm and is equipped with an interior thermometric probe.

Deeply desulphurized Light Cycle Oil (DLCO) which was prepared by hydrotreatment of pure Light Cycle Oil (LCO) using a commercial HDS catalyst ($NiMoP/Al_2O_3$ from Axens) was used as the feedstock. LCO is a middle distillate refinery product generated in a fluid catalytic cracking (FCC) unit. The main properties of DLCO are summarized in Table 3. DLCO has a very low sulphur content and a relatively high aromatic content. The sulphur content of this feed has been increased artificially up to 50 ppm S by adding dibenzothiophene (DBT). This procedure allows for evaluating the HDS activity and the effect of the amount of sulphur on the hydrogenating properties of the catalysts for the same composition of aromatics in the feed.

DLCO hydrogenation was carried out under the following conditions: total pressure 6 MPa, reaction temperature 300 °C, liquid-hourly space-velocity (LHSV) 1 h^{-1}, hydrogen-to-feed ratio (without recycling) 450 NL/L. The 1Pt(Cl)ZM-45 catalyst has been tested in two experiments: (1) the crushed sample, 30 ml (20.4 g) of sample with fraction 4–8 mm and diluted in 10 ml of SiC (0.8 mm); (2) the monolithic sample, 8 pieces (30 ml, 18.8 g).

The catalyst was dried in situ under pure H_2 flow for 4 h at 150 °C before being reduced at 300 °C for 2 h. After reduction, the catalyst was cooled down to 150 °C. Then, DLCO containing 20 ppm sulphur (from DBT) was introduced and the test conditions were adjusted. The change of feedstock containing

Table 3
DLCO composition and performance of 1Pt(Cl)ZM-45 catalyst in hydrogenation of desulphurized Light Cycle Oil (6 MPa, 300 °C, LHSV 1 h^{-1}, and hydrogen-to-feed ratio 450 NL/L).

Catalyst	*S* in feed (ppm)	Hours on stream	H (wt.%)	CN	MA (wt.%)	PA (wt.%)	TA (wt.%)	*S* (ppm)	*D* 15 °C	k_a (h^{-1})
DLCO Feed	1.2	–	12.66	35	30	2.2	32.2	–	0.8646	–
Crushed	20	132	13.20	32.9	17.14	1.03	18.17	0	0.8305	0.57
	20	144	13.20	32.8	17.28	1.04	18.32	0	0.8304	0.56
Crushed	50	312	12.96	31.2	22.19	1.32	23.51	0	0.8353	0.32
	50	324	12.96	30.9	22.66	1.37	24.03	0	0.8352	0.29
Monolith	50	336	12.79	30.2	25.32	1.61	26.93	2	0.8405	0.18
	50	348	12.79	30.1	25.66	1.63	27.29	3	0.8406	0.17

H—hydrogen, wt.%; CN—cetane number; MA—monoaromatics, wt.%; PA—polyaromatics, wt.%; TA—total aromatics, wt.%; *D*—density at 15 °C.

50 ppm sulphur (from DBT) was implemented after the performance stabilization.

The experiment was followed by measuring the product density (D) every twelfth hour. When the density was stabilized, the percentage and type of aromatics (Total Aromatics (TA), Mono Aromatics (MA) and Poly Aromatics (PA)) in the products were measured by UV spectroscopy (Burdett method). The Cetane Number (CN) was determined by near infrared (NIR) spectroscopy referring to ASTM D613 (cetane motor). The percentage of Hydrogen (H) was also determined by NIR spectroscopy referring to the IFP method based on NMR measurements. The total amount of Sulphur (S) was measured by X-ray fluorescence. Simulated distillations (ASTM D86) were also carried out using the products.

The decrease in the total aromatic content in DLCO was assumed to be a pseudo-first-order reaction. The rate constant was defined by the following equation:

$$k_a\,(h^{-1}) = \ln(C_{\text{feed}}/C_{\text{product}}) \times \text{LHSV},$$

where C_{feed} and C_{product} are the concentration of aromatics in the feedstock and the product, respectively.

3. Results

3.1. Properties of zeolite-monoliths

The zeolite-containing monoliths prepared by extrusion of H-ZSM-5 powder with Ca-montmorillonite have a bimodal structure and developed specific surface area, reaching 330–350 $m^2\,g^{-1}$ (Table 1) even after introduction of the montmorillonite additive in 35 wt.% concentration. The microporous structure of the zeolite-containing monolith is formed by the channel system of the ZSM-5 zeolite (Fig. 1). Its pore volume and channel size are close to 0.1 $cm^3\,g^{-1}$ and 0.54–0.56 nm, respectively. The zeolite crystallites (0.5–1.0 μm) are connected into small agglomerated units between 4 and 18 μm in size that are covered by a thin montmorillonite film (Fig. 1). The space between the crystallites and between the agglomerated units forms the mesoporous structure of a material ($V\mu$ = 0.26–0.36 $cm^3\,g^{-1}$, $D \sim 4.5$ nm) and a small amount of transport pores (V = 0.15–0.20 $cm^3\,g^{-1}$, $D_{ef} \sim 110$ nm) [50]. In this way an attractive architecture of the pore space is realized.

The zeolite substrates are characterized by proton acidity. The concentration and strength of the acid sites can be regulated by changing of the zeolite/montmorillonite ratio in the extrusion mass and the zeolite Si/Al ratio [50]. FTIR spectroscopy showed that the zeolite-monolithic materials had high proton acidity characterized by Bronsted acid sites observed as absorption bands at 3610 (Al(OH)Si groups), 3665 (AlOH groups), and 3740 (SiOH groups) cm^{-1}. The spectral shift of the OH bands at 3610–3615 cm^{-1} due to interaction with CO was 320–340 cm^{-1} for the zeolite-monoliths compared to 260–290 cm^{-1} for pure HZSM-5. The proton acidity of OH groups, PA(OH), for the zeolite-monoliths was 1120–1160 kJ/mol. FTIR spectroscopy of chemisorbed CO recorded at 77 K showed absorption band (a.b.) at 2174 cm^{-1} attributed to vibrations of CO molecules H-bonded with OH groups.

We suppose that the physicochemical properties of the zeolite substrate: high surface area, developed pore structure with enough micro- , meso- and macropore volume, proton acidity, high mechanical strength, make them very attractive supports for Pt catalysts for deep desulphurization of diesel fuel. Besides, the bimodal texture of the developed zeolite substrates allows realizing a concept for design of sulphur-resistant noble metal hydrotreating catalyst proposed by Song [10,42]. According to this concept, noble-metal particles located in the micropores (<5 Å) and in large pore openings (>6 Å) provide for the sulphur resistance and desulphurization-hydrogenation activity, respectively. It was noted that the alumina and silica monoliths extruded with montmorillonite (Table 1) do not have the necessary textural properties. They have lower surface areas (129–162 $m^2\,g^{-1}$) and larger mesopore diameters (9–15 nm) compared to the zeolite-monoliths. The monoliths based on alumina, silica or Y zeolite extruded with montmorillonite and ZSM-5 extruded with alumina are also characterized by low proton acidity.

3.2. Morphology of Pt particles in Pt-zeolite catalysts

The morphology, location and size distribution of Pt particles have been investigated by TEM. The TEM micrographs of different Pt-zeolite catalysts are shown in Fig. 2. According to different contrast in the TEM micrographs we observed coffin-shaped zeolite crystallites (with length 300–500 nm and width 150–200 nm), laminated structure of montmorillonite and Pt particles. The Pt particles were located both on the montmorillonite and the zeolite crystallite surfaces. The shape, size and distribution of Pt particles depended on the preparation method.

When Pt catalyst was prepared by ion-exchange with the $Pt(NH_3)_4Cl_2$ solution, we observed two types of Pt particles (Fig. 2a and c). The particles of one type were finely dispersed with roundish shape and prevalent size 2–5 mn, and were uniformly distributed on the catalyst surface. However, it was not possible to determine the state of Pt (Pt^0 or PtO or PtO_2) in the small particles and their location (inside the zeolite channels or on the outside surface). The particles of the second type were well crystallized Pt^0 particles with prismatic shape and prevalent size 10–25 mn. The large Pt^0 crystallites were located on the outside surface of the zeolite crystals. The concentration of these large crystallites was much higher in Pt-ZSM-5 catalysts with high Pt content, especially in the samples without montmorillonite (Fig. 2a).

When the Pt catalyst was prepared by incipient wetness impregnation with H_2PtCl_6 solution, we observed a narrow particle size distribution (1–3 nm). Still, these Pt particles were non-uniformly distributed on surface. Most of them were concentrated close to the defect (footstep) of the montmorillonite surface and to the edges of the zeolite crystallites (Fig. 2b and d). The size of Pt

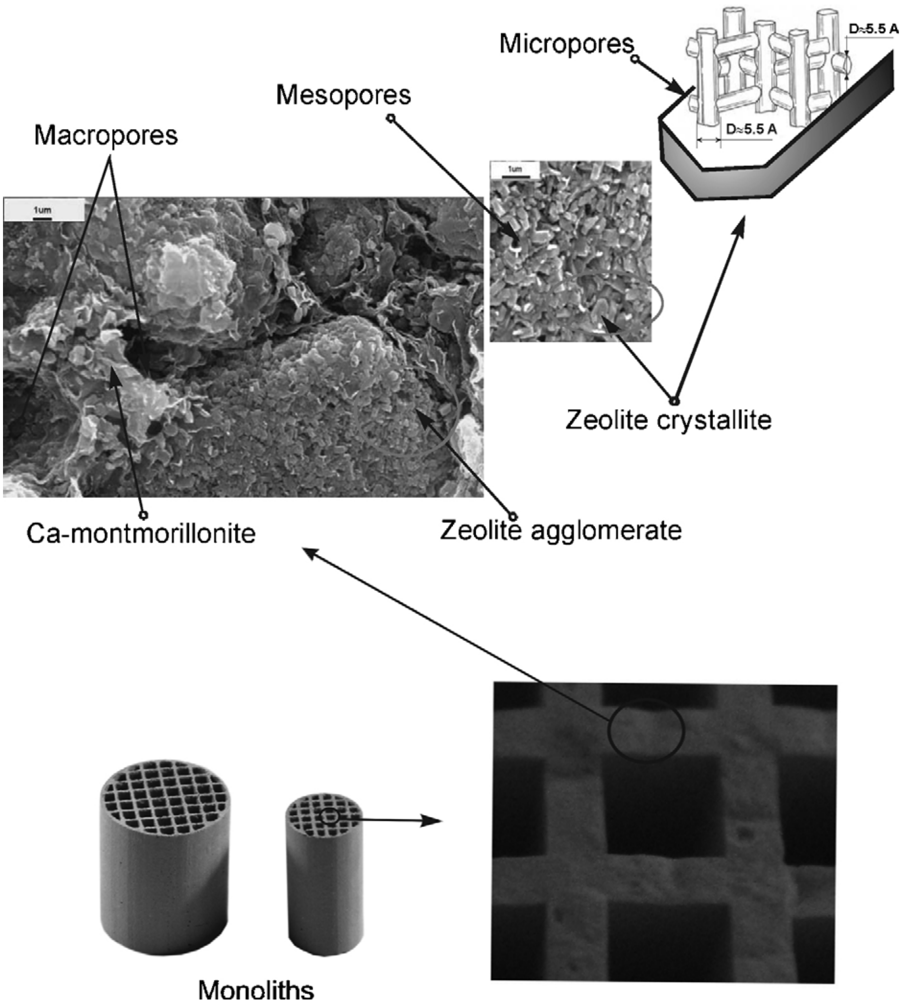

Fig. 1. SEM micrographs of the wall of zeolite-monolithic substrate and scheme of the pore structure.

particles in the impregnated catalyst increased (up to 3–10 nm) after reduction in hydrogen (Fig. 2e).

The zeolite Si/Al ratio also affected the shape and size of Pt particles. The shape of Pt particles changed from flat to roundish and their size increased with the growth of the Si/Al ratio from 17 to 30–45. With increasing Si/Al ratio, the acidic strength of HZSM-5 increases, while the concentration of Bronsted acid sites decreases. These results suggest that the size and shape of Pt particles depend on the support acidity, and they are determined by the strength of the interaction between the Pt particles and the support.

Note that both the impregnated and the ion-exchanged Pt catalysts can contain Pt as particles with size 1–2 nm inside the zeolite channels, which are not visible by TEM. According to the data published in [51,52], the maximum size of Pt particles located inside the ZSM-5 zeolite channels is around 3.5 nm.

3.3. *States of Pt in Pt-zeolite catalysts, FTIR of adsorbed CO*

The states of Pt were studied by XRD, FTIR spectroscopy of adsorbed CO, XPS, and EXAFS as a function of the support chemical composition, the nature of the Pt precursor, its loading, and the catalyst preparation method.

The coordinatively unsaturated sites in nanostructured Pt catalysts were monitored by FTIR spectroscopy of chemisorbed CO. The stretching frequencies and relative intensities of the CO bands are known to be sensitive to the oxidation state [53], particle size [51,54–58], and the metal-support interaction [53,59], and can be used for characterization of the electronic state of Pt in supported catalysts.

The FTIR spectra of our Pt-zeolite catalysts showed the bands at 3745, 3610, and 3700 cm^{-1} in the O-H stretching region. The first two bands were observed for H-ZSM-5 and assigned to the O-H stretching of silanol groups and zeolite bridged hydroxyls, respectively. The band at 3700 cm^{-1} probably corresponds to the O-H stretching of Pt(OH) groups [60].

Fig. 3 shows the FTIR spectra of CO adsorbed on Pt catalysts supported on the zeolite powder (a and b) and zeolite-monoliths (c, d, e) at room temperature. For Pt catalysts prepared by different methods (Fig. 3), an intensive asymmetric absorption band at 2070–2100 cm^{-1} with a shoulder at 2050–2065 cm^{-1} was observed in the FTIR spectra of adsorbed CO. In addition, high frequency bands at 2122, 2149-2155 and 2196 cm^{-1} were recorded in the FTIR spectra of the ion-exchanged Pt-zeolite catalysts (Fig. 3a and c). An additional band at 2134–2136 cm^{-1} was found in the FTIR spectra of the impregnated Pt-catalyst on zeolite-montmorillonite monoliths (Fig. 3d and e). Note that the above-mentioned adsorption bands were not observed in the spectra of H-ZSM-5 and HZSM-5 with montmorillonite without Pt.

The asymmetric peak is likely a superposition of the absorption bands with the maxima at 2055–2065 and 2090–2095 cm^{-1}. The band at 2090 cm^{-1} is usually assigned to Pt^0-CO species produced with participation of finely dispersed platinum about 3–5 nm in size [53–59]. The band at 2070 cm^{-1} can be assigned to Pt^0-CO carbonyls formed on larger platinum particles resulting from CO-

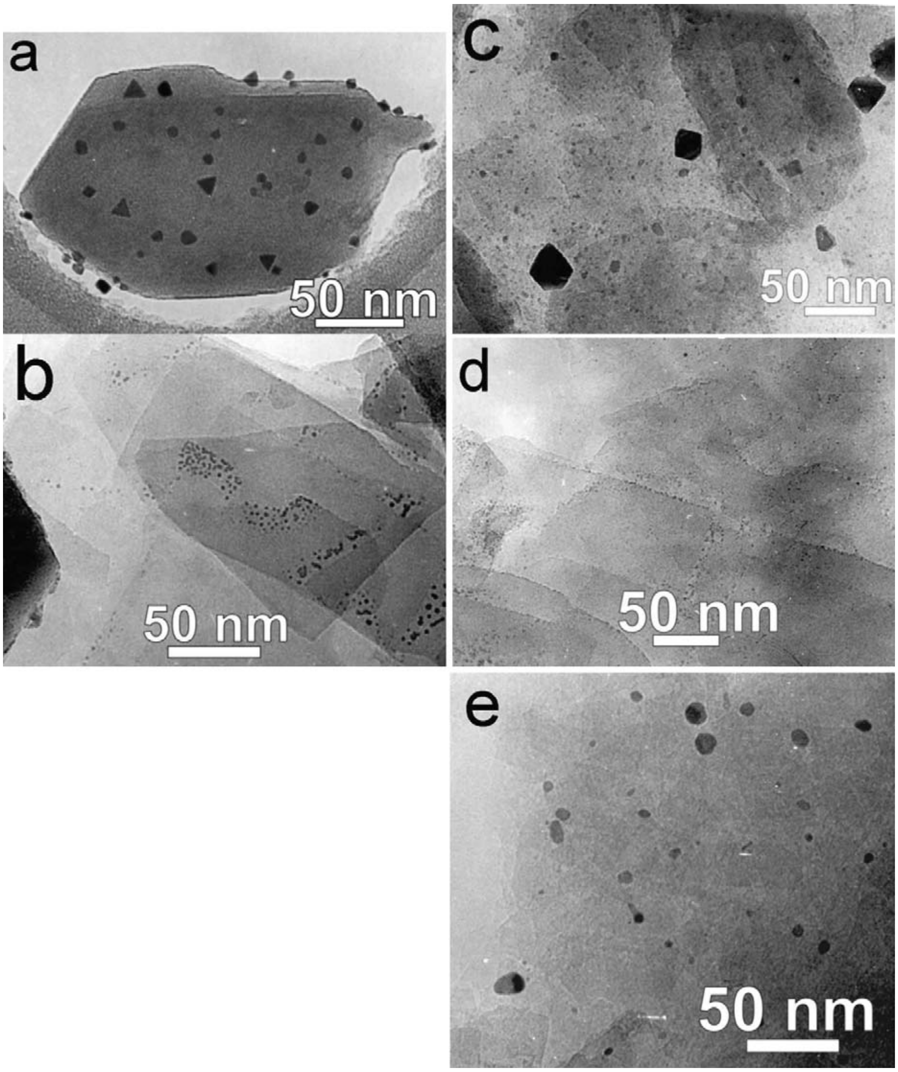

Fig. 2. HRTEM micrographs of ion-exchanged ((a) and (c)—fresh) and impregnated ((b) and (d)—fresh, (e)—reduced) Pt-catalysts based on the zeolite-monolith ZM-45 ((c)—(e)) and zeolite H-ZSM-5 (a) and (b).

induced platinum agglomeration [57,58]. Based on the literature data, the band at 2050–2055 cm^{-1} can be assigned either to CO molecules linearly adsorbed on big Pt metal particles with the size 10–50 nm on the outside surface [57,61] or to CO molecules linearly adsorbed on small Pt metal particles with the size 1–2 nm [58]. The difference between the vibration frequencies of CO molecules linearly adsorbed on Pt metal (changed from 2050 to 2095 cm^{-1}) is basically explained by the change of the electronic properties of superficial platinum atoms [57,61,62]. The electronic properties of platinum atoms, apparently, depend on their interaction with the support [57,59,62–64], and consequently, on the preparation route of Pt catalysts and acidic properties of the supports. In our case, the a.b. at 2055–2065 cm^{-1} was more intensive for the impregnated catalysts on H-ZSM-5 powder, for example, 1Pt(Cl)Z-45 sample (Fig. 3b). The a.b. at 2090–2095 cm^{-1} was more intensive for the ion-exchanged Pt catalyst (Fig. 3a and c) and for the impregnated Pt catalysts on the support with the montmorillonite additive. Its intensity increased with the Pt loading. The intensity of these absorption bands at 2055–2065 and 2090–2095 cm^{-1} did not significantly change during the desorption process. This indicates that there was strong interaction of the CO molecules with the Pt particles. The band at 2090–2095 cm^{-1} shifted to low frequency during the CO desorption, which is typical of the Pt metal [61,62]. The Pt particles smaller than 5 nm were observed by TEM on the outside surface of the impregnated sample (Fig. 2b and d). The ion-exchanged sample had both 2–5 nm and 10–25 nm particles (Fig. 2a and c). The acidity of H-ZSM-5 significantly increases when Ca-montmorillonite was added to the zeolite supports (Table 4). In agreement with the TEM and acidity data, we suppose that the absorption bands at 2055–2065 and 2090–2095 cm^{-1} are related to small Pt metal particles varying by location and interaction with the support.

The absorption bands at 2122, 2149–2155 and 2196 cm^{-1} could be clearly detected on the ion-exchanged Pt-zeolite catalysts (Fig. 3a and c), when the formation of charged cations and atomically dispersed metal species is possible [59,65,66]. The carbonyl bands at high stretching frequencies have been assigned to the oxidized Pt species [53–55,57,58,61–64]. The observed bands can correspond to CO molecules adsorbed on the positively charged monoatomic Pt species. The band at 2195 cm^{-1} is probably due to Pt^{3+} [58], the band at 2150 cm^{-1} is due to Pt^{2+} [51,57], and the band at 2122 cm^{-1} is due to the partially positively charged Pt species coordinated to the charged zeolite sites [57,58]. The a.b. 2113–2128 cm^{-1} and 2150 cm^{-1} can also describe vibrations of CO adsorbed on Pt^{2+} as monocarbonyl [57,58] and bicarbonyls [57], respectively.

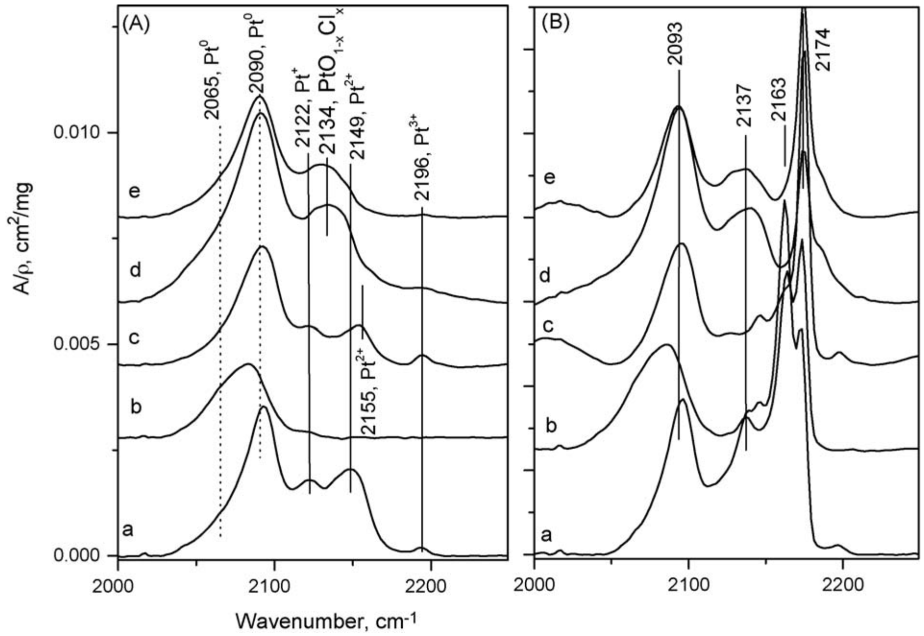

Fig. 3. FTIR spectra of chemisorbed CO (A, 25 °C; B, −196 °C) on the ion-exchanged ((a) and (c)—fresh) and the impregnated ((b) and (d)—fresh, (e)—reduced) Pt-zeolite catalysts: (a) 1.2Pt(A)Z-45; (b) 1.2Pt(Cl)Z-45; (c) 1.6Pt(A)ZM-45; (d) and (e) 1.8Pt(Cl)ZM-45.

The absorption band at 2134–2136 cm^{-1} is more intensive on the impregnated Pt-zeolite catalysts (Fig. 3d), when the formation of dispersed PtO_x species doped by Cl^- ions [67–69] on the surface is possible. These absorption bands can also correspond to CO molecules adsorbed on the positively charged monoatomic Pt species, for example, Pt^+-CO [57,58].

The observation of the bands at 2090–2095 cm^{-1} and 2122 cm^{-1} in the FTIR spectra of the ion-exchanged Pt catalysts suggests that both bands can be assigned to electron-deficient Pt atoms anchored to the zeolite by one or two acidic hydroxyl group located inside the zeolite channels. Similar results were discussed by Zholobenko for Pt-mordenite [64] and by Stakheev for Pt-ZSM-5 [61]. This assumption is supported by the experimental data because the observation of the band at 2122 cm^{-1} depends on the preparation route and acid properties of the support, namely it is mainly observed in the FTIR spectra of ion-exchanged zeolite. In this case, the bands at 2095 cm^{-1} and 2122 cm^{-1} would correspond to the asymmetric and symmetric vibrations of dicarbonyl adsorbed on highly unsaturated Pt atoms [61].

In addition to the adsorption bands mentioned above, we observed adsorption bands at 2137–2142, 2146, 2163–2175, and 2186–2196 cm^{-1} in the FTIR spectra of adsorbed CO recorded at −196 °C (Fig. 3B). The adsorption band at 2186–2196 cm^{-1} is likely caused by the vibrations of CO adsorbed on different Lewis acid sites, such as Al^{3+} (a.b. 2196 cm^{-1}), Ca^{2+} (a.b. 2188 cm^{-1}), Fe^{3+}, Mg^{2+} and others present in Ca-montmorillonite. The adsorption band at 2163–2175 cm^{-1} is produced by vibrations of CO associated with the surface OH groups by a weak hydrogen bond.

For the Pt catalysts on the support with montmorillonite, the spectral shifts of OH bands at 3612 and 3740 cm^{-1} due to interaction with CO were 120–130 cm^{-1} and 65–80 cm^{-1}, respectively. The proton acidity of the strongest OH groups (3612–3615 cm^{-1}) in these Pt-zeolite-monoliths was 1320–1330 kJ/mol. The proton acidity of the strongest OH-groups (3612–3615 cm^{-1}) of the impregnated and ion-exchanged Pt-HZSM-5 catalysts was equal to 1295 kJ/mol and the spectral shift was 140–165 cm^{-1}. The experimental data indicate that the proton acidity of the Pt catalysts supported on both HZSM-5 powder and monoliths was very low in comparison with the ones of H-ZSM-5 and H-ZSM-5 with montmorillonite (1120–1160 kJ/mol). So, the acidic properties of the zeolite support were modified by supporting the metal particles.

The adsorption bands at 2137–2138 cm^{-1} (specific to Pt-zeolite) and 2142–2146 cm^{-1} (specific to Pt-zeolite-montmorillo-

Table 4
Concentrations of Pt sites on the monolith surface according to FTIR data.

Catalyst	PA(OH) for a.b. 3612 cm^{-1} (kJ/mol)	CO absorption site							
		Pt^0-CO			Pt^+-CO		Pt^{2+}-CO		Pt^{3+}-CO, 2196
		ν_{CO} (cm^{-1})	C_s (μmol g^{-1})	C_{FTIR}/C_{ICP}	ν_{CO} (cm^{-1})	A/A*	ν_{CO} (cm^{-1})	A/A*	A/A*
Z-45	1210	–	–	–	–	–	–	–	–
ZM-45	1160	–	–	–	–	–	–	–	–
1Pt(Cl)ZM-17	1260	2095	32	0.63	2128	1.0	–	–	–
1Pt(Cl)ZM-30	1230	2091	37	0.72	2125	1.0	2146	1.25	–
1Pt(Cl)ZM-45	1210	2090	43	0.84	2118	1.0	2131	1.0	–
2Pt(Cl)ZM-45	1347	2091	18	0.19	2129	–	2138	0.9	4.5
2Pt(Cl)ZM-45 reduced in H_2	1352	2088	9	0.10	2129	–	2134	0.6	–
2Pt(A)ZM-45	1356	2091	9	0.11	2124	2.0	2151	0.65	1
1Pt(Cl)Z-45	1290	2083	6	0.10	2119	0.08	–	–	–
1Pt(A)Z-45	1290	2093	11	0.18	2122	2.0	2149	1.75	2.5

A/A*—relative value calculated as a ratio between the areas of absorption band of the indicated sample and the sample which area is taken equal to 1.

nite) in the FTIR spectra recorded at −196 °C are due to CO condensed in the pores, most likely in the zeolite pores. The observation of the a.b. at 2137–2142 $\mathrm{cm^{-1}}$ proves that the zeolite micropores are available for CO molecules and probably for other small molecules, for example, hydrogen.

So, the FTIR spectroscopy of adsorbed CO shows that Pt catalysts supported on zeolite-monoliths contain Pt in two oxidation states: Pt metal particles of different sizes (a.b. 2070–2090 $\mathrm{cm^{-1}}$) and oxidized $\mathrm{Pt^{\delta+}}$ species (a.b. 2128 and 2150 $\mathrm{cm^{-1}}$). The concentrations of these Pt states depend on the Pt precursor, Pt loading, presence of montmorillonite and pre-treatment conditions. Table 4 shows the relative concentrations of different states of Pt observed on the surface of the Pt-catalysts. These data led us to the following conclusions.

First, at the same Pt loading (1.2 wt.%) the use of $\mathrm{Pt(NH_3)_4Cl_2}$ or $\mathrm{H_2PtCl_6}$ solution as the Pt precursor promotes stabilization of $\mathrm{Pt^0}$ particles of different sizes. The impregnated Pt catalysts have smaller $\mathrm{Pt^0}$ particles in comparison with the ion-exchanged Pt catalysts.

Second, the use of different precursor results in the formation of different types of oxidized $\mathrm{Pt^{\delta+}/Pt^{2+}}$ species. When $\mathrm{Pt(NH_3)_4Cl_2}$ was used for the catalyst preparation we observed the formation of the oxidized $\mathrm{Pt^{\delta+}/Pt^{2+}}$ species, probably inside the zeolite channels close to the cation-exchanged zeolite site (a.b. 2122–2124 and 2150–2155 $\mathrm{cm^{-1}}$). When $\mathrm{H_2PtCl_6}$ was used for the catalyst preparation the oxidized $\mathrm{Pt^{\delta+}/Pt^{2+}}$ species were the PtO-species doped by Cl-ions, e.g. like to $\mathrm{PtO_{1-x}Cl_x}$ (a.b. 2134–2146 $\mathrm{cm^{-1}}$).

The increase of the Pt loading (from 1.0 to 1.8 wt.% Pt) decreases the concentration of the FTIR-visible Pt species. The amount of $\mathrm{Pt^0}$ particles decreases more significantly, whereas the amount of oxidized Pt species does not considerably change. As mentioned above, the formation of more oxidized Pt species, such as $\mathrm{Pt^{3+}}$, takes place when the Pt loading in the impregnated catalysts is doubled. The most part of the oxidized Pt species transform to $\mathrm{Pt^0}$ during reduction of the Pt catalysts in $\mathrm{H_2}$-containing feed at 400 °C.

The presence of Ca-montmorillonite in the catalyst promotes the formation of the oxidized Pt-species: $\mathrm{Pt^{\delta+}}$ and $\mathrm{Pt^{2+}}$, independent of the Pt precursor. The formation of more $\mathrm{Pt^{\delta+}/Pt^{2+}}$ ions in the montmorillonite-containing catalysts can be explained by strong interaction of platinum particles with OH groups of the support that changes the electronic properties of superficial Pt particles.

The ratio between the concentrations of Pt observed by FTIR as $\mathrm{Pt^0}$-CO at 2070–2090 $\mathrm{cm^{-1}}$ and that obtained by the chemical analysis (denoted as C_s^{FTIR}/C_s^{ICP}) was calculated. It was shown that the FTIR-visible part of Pt was as high as 0.6–0.8 in the catalysts containing 1 wt.% of Pt. These experimental data suggest that these catalysts contain Pt as finely dispersed particles. However, this ratio decreased to 0.2 when the Pt loading was doubled. The most significant decrease of this ratio was observed for reduced Pt catalysts, indicating the increase of the $\mathrm{Pt^0}$ particle size.

3.4. States of Pt in Pt-zeolite catalysts, XPS

The investigation of Pt-zeolite supported systems by means of XPS has some spectroscopic obstacles. First of all, the most intensive platinum line Pt4f, usually used for XPS analysis of Pt oxidation states, lies in the region in XPS-spectra with very intensive Al2p line of alumina from zeolite. As a consequence, to get the reliable information about platinum states in Pt-Al systems is very difficult. The analysis of Pt4d lines is possible, but the low intensity of this line leads to a decrease of analysis precision and to a limitation of minimal Pt loads in the samples (not less than 1 wt.%). In the present work, analysis of both Pt4f- and Pt4d- core lines was used for investigation of platinum oxidation states. Examples of difference spectra of $\mathrm{Pt4f_{7/2}}$ and Pt $\mathrm{4d_{5/2}}$ for 1.1Pt(Cl)ZM-45 and 1.2Pt(Cl)Z-45 samples are presented in Fig. 4.

The binding energy of $\mathrm{Pt4f_{7/2}}$ line, received from the difference spectra of 1.1Pt(Cl)ZM-45 catalyst and ZM-45 support, is $\mathrm{BE(Pt4f_{7/2})}$ = 72.5 eV (Fig. 4a). It is a typical BE for the platinum in oxidized state like $\mathrm{Pt(OH)_2}$ or $\mathrm{Pt_2Si}$. Formation of $\mathrm{Pt_2Si}$ is not

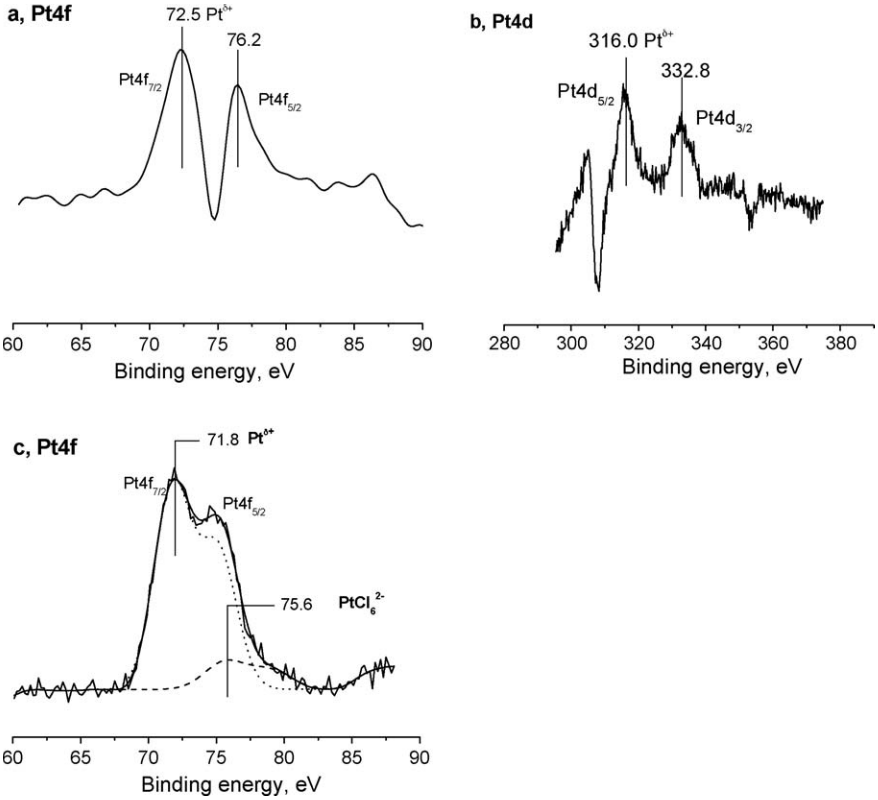

Fig. 4. The difference XPS spectra of Pt4f ((a) and (c)) and Pt4d (b) for 1.2Pt(Cl)/ZM-45 ((a) and (b)) and 1.2Pt(Cl)/Z-45 (c).

possible in the used mild thermal pre-treatment conditions. It should be noted that this BE of Pt4$f_{7/2}$ line might be caused by nano-size effect of metal platinum particles. Pt4d peaks are also well-defined in the difference spectra. For the sample 1.1Pt(Cl)/ZM-45 the binding energy for Pt 4$d_{5/2}$ is 316.0 eV (Fig. 4b). This binding energy may be ascribed to platinum in the oxidized state or to highly dispersed metallic particles (BE of Pt4$d_{5/2}$ for the Pt-metal is 314.6 eV).

For the samples 1.2Pt(Cl)Z-45 and 1.2Pt(A)Z-45 the HWMH (Half Width on the Middle Height) of Pt4$f_{7/2}$ line was quite large, so the Pt4f and Pt4d spectra were decomposed to some individual states. For the 1.2Pt(Cl)Z-45 sample this is shown on Fig. 4c. It is clear that in this sample there are two different states of platinum, corresponding to two doublets with BE(Pt4$f_{7/2}$) = 71.8 eV and BE(Pt4$f_{7/2}$) = 75.6 eV. Most part of platinum in the 1.2Pt(Cl)Z-45 sample has an effective charge δ+ (BE = 71.8 eV). Probably it is platinum present in small Pt-clusters, containing Pt–Pt bonds inside and Cl in a stoichiometry Cl/Pt ≈ 1/1. Additional platinum species are present in $PtCl_6^{2-}$ (BE = 75.6 eV). Pt4d spectra also contain two doublets with BE = 314.9 eV and BE = 318.1 eV, corresponding to platinum with δ+ and oxidized platinum in $PtCl_6^{2-}$.

The Pt4f XPS spectra from the ion-exchanged and impregnated Pt-zeolite catalyst are shown in Fig. 5 while numerical values of the binding energy (BE) of Pt 4$f_{7/2}$ and Pt 4$d_{5/2}$ are summarized in Table 5. One can see that the BE of Pt 4$f_{7/2}$ shifts to higher values (to 71.8–72.5 eV) for all calcined Pt-catalysts in comparison to that of metallic platinum crystallites (Pt^0, 71.1 eV [70]). This shift indicates a more oxidized state of the Pt particles than Pt^0. The shift of the BE is more pronounced on Pt-catalysts which possessed higher acidity of zeolite support, namely, zeolite with montmorillonite additive. The BE was 72.3–72.5 eV for Pt(Cl)ZM-45 and 71.8 eV for Pt(Cl)Z-45. The BE of Pt 4$f_{7/2}$ corresponding to Pt^0 is observed only after Pt-catalyst reduction in hydrogen at 400 °C and for the Pt(A)Z-45 sample calcined in air at 400 °C. Significant enrichment of the catalyst surface with platinum is observed for all Pt-zeolite catalysts, because their Pt/Si surface atomic concentration ratios calculated from XPS are higher than their Pt/Si volumetric atomic ratios calculated from AAC-ICP (Table 5).

It was also shown by XPS that the main Pt states, such as Pt^0 and $Pt^{\delta+}$, in the nanostructured ion-exchanged and impregnated catalysts prepared by using of $Pt(NH_3)_4Cl_2$ and H_2PtCl_6, respectively, depend on the zeolite Si/Al ratio, the montmorillonite additive and the Pt precursor.

First, the stabilization of the oxidized state of Pt-particles, $Pt^{+\delta}$, with BE of Pt 4$f_{7/2}$ and Pt4$d_{5/2}$ equal to 72.5 eV and 315.0 eV, respectively, was observed when the Ca-montmorillonite additive and H_2PtCl_6 were used for synthesis of the Pt catalyst. For example, all impregnated Pt catalysts on zeolite-monoliths exhibited a higher Pt 4$f_{7/2}$ binding energy, 72.5 eV. The oxidized states are $Pt(OH)_2$ or Pt metal particles with the size smaller than 1 nm. In survey XPS spectra (Cl2p line) the chlorine-ion was observed, indicating that the modification of Pt-species and zeolite surface by Cl-ions is possible.

On the other hand, the impregnated Pt catalysts on H-ZSM-5 powder (e.g. Pt(Cl)Z-45) contain two Pt states that can be ascribed to Pt^{+1} and Pt^{+4}, respectively. The former state has a BE of Pt 4$f_{7/2}$ and Pt 4$d_{5/2}$ equal to 71.8 eV and 314.9 eV, respectively, and it is probably represented by Pt clusters containing a Pt–Pt bond and Cl-ions with stoichiometry Pt/Cl = 1. The second one has a BE of Pt 4$f_{7/2}$ 75.6 eV and BE of Pt 4$d_{5/2}$ 318.1 eV. Most likely, this is a $[PtCl_6]^{2-}$ anion, some of which were not decomposed completely during the catalyst thermal treatment in the oxygenated environment [69,71]. The comparison of these data suggests that higher support acidity leads to a more oxidized state of Pt. It evidences the interaction between the Pt particles and the zeolite support which was also observed for Pt-MOR [59].

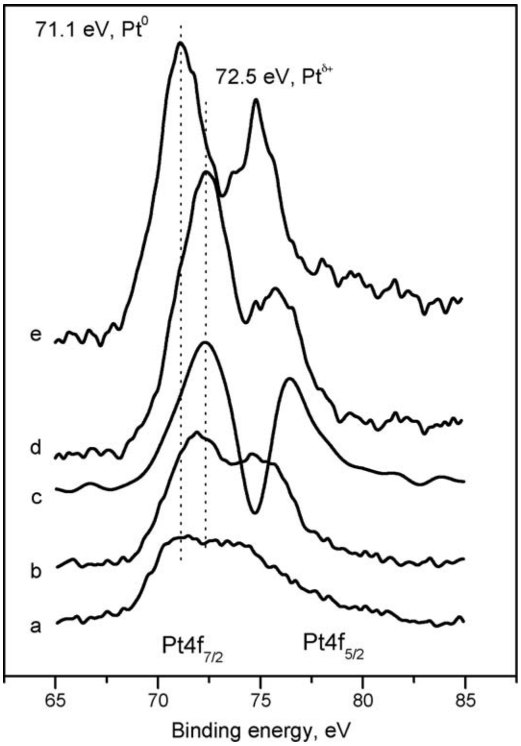

Fig. 5. The difference XPS spectra of Pt4f for Pt-zeolite catalysts: (a) 1.2Pt(A)Z-45; (b) 1.2Pt(Cl)Z-45; (c) 1.1Pt(Cl)ZM-45; (d) and (e) 1.8Pt(Cl)ZM-45 ((d)—fresh, (e)—reduced)).

Second, the formation of Pt^0 state with BE of Pt 4$f_{7/2}$ and Pt4$d_{5/2}$ equal to 71.1 eV and 314.8 eV, respectively, is favoured by a low support acidity and $Pt(NH_3)_4Cl_2$ as the precursor. For example, the ion-exchanged Pt-catalysts contain two Pt states. The main state has a BE of Pt 4$f_{7/2}$ 71.1 eV and BE of Pt 4$d_{5/2}$ 314.9 eV, which is typical of Pt metal [70]. The second state has a BE of Pt 4$f_{7/2}$ 75.1 eV corresponding to Pt in hydro/oxo or chloride complexes $Pt(OH)_6^{2-}$ or $PtCl_4$. The chlorine-ion was also observed in survey XPS spectra (Cl2p line), but its quantity was lower than in impregnated Pt-catalysts.

The impregnated catalyst on H-ZSM-5 has higher binding energy (71.8 eV) than the ion-exchanged catalyst (71.1 eV). This is attributed to the relatively smaller size of the active metal particles. The comparison of the ratio of the silicon and platinum XPS-peak areas shows that the Pt particles are bigger in the ion-exchanged catalyst 1.2Pt(A)Z-45 than in the impregnated catalyst 1.2Pt(Cl)Z-45. The statement about the distinction in the particle sizes also proves to be true regarding the intensity of Pt 4d lines. In the 1.2Pt(A)Z-45 sample the line is less intensive, indicating growth of the platinum particles. These data agree with the particle sizes observed by HRTEM, and can be easily explained by different concentrations of chlorine anions observed by XPS in the samples. It is known that chlorine prevents Pt from being aggregated into large particles [72–74].

Third, the most part of $Pt^{+\delta}$ species transform to Pt^0 during reduction in hydrogen at 400 °C ($BE_{Pt4f7/2}$ = 71.1 eV). The oxidized Pt state is also presented in very small quantity, which does not allow its identification.

3.5. States of Pt in Pt-zeolite catalysts, EXAFS

The curves of the radial distribution function (RDF) of atoms describing the Pt local arrangement in Pt-ZSM-5 and Pt-zeolite-monolith are shown in Fig. 6. The RDF curve of the platinum foil (reference) is also presented for comparison. The structural data

Table 5
Pt sites on the monolith surface according to XPS and EXAFS data.

N	Catalyst	AAS-ICP		XPS				EXAFS					
		Pt content (%)	Atomic Pt/Si ratio	Pt binding energy (eV)		Pt state	Atomic Pt/Si ratio	Pt–O		Pt–Cl		Pt–Pt	
				Pt $4f_{7/2}$	Pt $4d_{5/2}$			R (Å)	CN	R (Å)	CN	R (Å)	CN
1	1Pt(Cl)ZM-17	1.1	0.004	72.4	315.6	$Pt^{\delta+}$ as $Pt(OH)_2$ or Pt^0 (<10 Å)	n.d.						
2	1Pt(Cl)ZM-30	1.0	0.003	72.4	315.8	$Pt^{\delta+}$ as $Pt(OH)_2$ or Pt^0 (<10 Å)	n.d.						
3	1Pt(Cl)ZM-45	1.1	0.004	72.5	316.0	$Pt^{\delta+}$ as $Pt(OH)_2$ or Pt^0 (<10 Å)	0.013	–	–	2.29	2.6	2.77	2.6
4	2Pt(Cl)ZM-45	1.8	0.007	72.3	315.7	$Pt^{\delta+}$ as $Pt(OH)_2$ or Pt^0 (<10 Å)	0.042	–	–	2.31	4.3	~3.1–4.3	~1–2
5	2Pt(Cl)ZM-45 reduced in H_2	1.8	0.007	71.1	314.4	Pt^0	0.058						
6	2Pt(A)ZM-45	1.6	0.006	n.inv.	–	–	–	1.99	3.4	–	–	2.79	5.1
7	1Pt(Cl)Z-45	1.2	0.004	71.8 75.6	314.9 318.1	$Pt^{\delta+}$, Pt:Cl = 1:1 (~88 %) $PtCl_6^{2-}$ (~12%)	0.023	–	–	2.29	2.4	–	–
8	1Pt(A)Z-45	1.2	0.004	71.1 75.1	314.9 –	Pt^0 (~75%) $Pt(OH)_6^{2-}$, PtO_2 or $PtCl_4$(~25%)	0.019	2.01	3.6	–	–	2.79	2.5
	Pt-foil							–	–	–	–	2.77	11.8

Chlorine was observed in survey XPS spectra (Cl2p line) of all samples; R—Pt–O, Pt–Cl and Pt–Pt distances; CN—effective coordination number; n.inv.—the sample was not investigated by XPS or EXAFS; n.d.—not determined.

such as effective coordination numbers and distances for the Pt–O, Pt–Cl, Pt–Pt coordination spheres calculated from the EXAFS spectra for the local Pt arrangement are presented in Table 5.

Analysis of the RDF curves and calculated EXAFS data for our PtZ-45 and PtZM-45 samples led us to the following conclusions.

Addition of Ca-montmorillonite to the support, e.g. in samples 1.8Pt(Cl)ZM-45 and 1.2Pt(Cl)Z-45 prepared using the H_2PtCl_6 precursor, hinders the formation of platinum metal particles, Pt^0. However, addition of Ca-montmorillonite in the same amount in the case of 1.6Pt(A)ZM-45 prepared from $[Pt(NH_3)_4]Cl_2{\bullet}H_2O$ precursor is not sufficient to prevent formation of Pt^0 particles promoted by tetraammineplatinum chloride. In the 1.8Pt(Cl)ZM-45 and 1.2Pt(Cl)Z-45 catalysts platinum is present only in the form of a partially decomposed initial chloride complex and practically no platinum metal is observed. The distant peaks at 3.1–4.2 Å giving coordination numbers ~ 2 after fitting correspond to the distances R_{Pt-Pt} and R_{Pt-Cl} for far coordination spheres in the structures of platinum chloride and tetrachloroplatinates [75].

In the RDF curves of the samples 1.8Pt(Cl)ZM-45, 1.1Pt(Cl)ZM-45 and 1.2Pt(Cl)Z-45 there are peaks (for the first coordination sphere), which correspond to the distance Pt–Cl (~2.3 Å) typical of platinum-chloride systems [75]. The fitting data also confirm the presence of such distances. However, the obtained coordination numbers are somewhat low (CN = ~2.4, 4.2; Table 5) in comparison with the octahedral arrangement of Pt typical of platinum-chloride systems [75]. The lower values of the effective coordination numbers are most likely caused by small particle sizes and significant distortion of the octahedral chloride arrangement.

In the RDF curves of the samples 1.2Pt(A)Z-45 and 1.6Pt(A)ZM-45 there are peaks (for the first coordination sphere) that correspond to the distance Pt–O (~1.98–2.1 Å) typical of some oxide and hydroxide Pt systems [76]. The fitting data confirm the presence of such distances. Still, the obtained coordination numbers are again low (CN = ~4; Table 5) in comparison with the octahedral arrangement of Pt typical of platinum-chloride systems [75]. The lower values of the effective coordination numbers are related to the small size of particles with significant distortion of the octahedral oxygen arrangement.

It should be noted that in a number of samples, platinum is present in two forms. For instance, platinum metal Pt^0 was observed in addition to the "chloride" form for samples 1.8Pt(Cl)ZM-45 and 1.1Pt(Cl)ZM-45 and the "oxide" form for samples 1.2Pt(A)Z-45 and 1.6Pt(A)ZM-45. In the RDF curves of these samples there are far peaks corresponding to the first peak in the fcc structure typical of platinum metal [77] (Fig. 6). Such comparison was carried out using reference Pt-foil. However, noteworthy are the substantial differences in the amplitudes and some shifts in the positions of the peaks attributed to platinum metal in the RDF curves of the local arrangement for these samples (Fig. 6).

The fitting data (Table 5) also completely prove the above-mentioned finding. The calculated values of the effective coordination numbers for 1.1Pt(Cl)ZM-45 and 1.2Pt(A)Z-45 are ca. 2.5–2.6. These values indicate that there are significant distortions of the platinum metal structure and small dimensions of Pt^0 particles compared to the reference sample. The sample 1.6Pt(A)ZM-45 had rather high CN value equal to 5.1. This fact

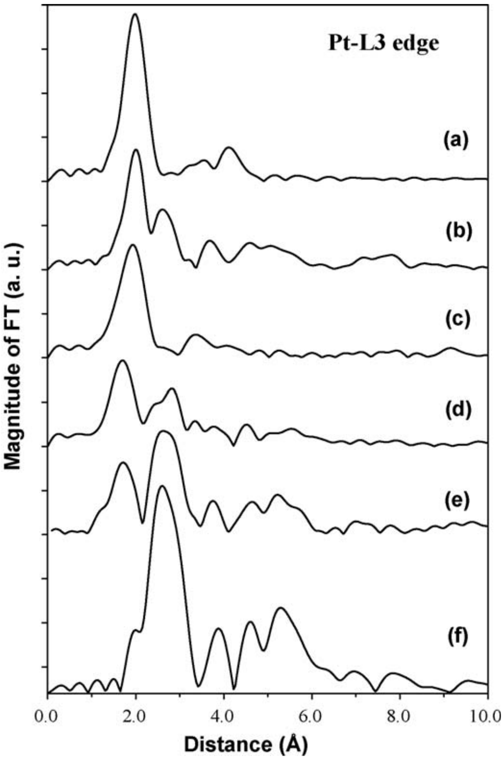

Fig. 6. Radial distribution function (RDF) curves describing Pt local arrangement for the studied samples calcined at 400 °C: (a) 1.8Pt(Cl)ZM-45; (b) 1.2Pt(Cl)Z-45; (c) 1.1Pt(Cl)ZM-45; (d) 1.2Pt(A)Z-45; (e) 1.6Pt(A)ZM-45; (f) Pt-foil (reference).

indicates that platinum particles Pt^0 in this sample are larger and more ordered in comparison with the other samples. Better structure ordering in this sample compared to the samples 1.1Pt(Cl)ZM-45 and 1.2Pt(A)Z-45 is also confirmed by the growth in intensity of the distant peaks attributed to Pt–Pt distances 3.5–6.5 Å.

3.6. Catalytic activity

The effect of catalyst chemical compositions, the state of Pt and support acidity on the hydrodesulphurization and hydrogenation activity of supported Pt catalysts was studied.

Three main products were observed in the hydrodesulphurization of thiophene over Pt-zeolite: hydrogen sulphide, C_4-hydrocarbons (such as butane and butene) and fully hydrogenated sulphur-containing intermediate tetrahydrothiophene (C_4H_8S). Fig. 7 shows the rates of thiophene conversion to C_4-hydrocarbons and tetrahydrothiophene over 1Pt(Cl) ZM-45 catalyst. The formation rate of desulphurized C_4-products decreased with time and achieved a steady-state value in 30–40 min. The tetrahydrothiophene formation rate increased and also reached a constant value after same time, indicating that desulphurization of the fully hydrogenated sulphur-containing intermediate is unfavourable over Pt-zeolite at 300 °C and pressure 20 atm.

The catalytic results obtained over our Pt-zeolite catalysts for the thiophene HDS reaction, in terms of total thiophene conversion, rate of thiophene conversion, selectivity to C_4-hydrocarbons via the HDS route, and selectivity of tetrahydrothiophene formation via the HYD route are summarized in Table 2. Our Pt-zeolite-monolithic catalysts exhibit fair activity in thiophene HDS, which achieved 1700–3400 moles of C_4H_4S per mole of Pt per hour at 300 °C. The high thiophene and DBT hydrodesulphurization activity and sulphur resistance were reported for Pt on H-ZSM5 [78,79] and Y [36,78–80] zeolites and ASA [22,25,81].

The steady-state activity of Pt-zeolite-monolithic catalysts in thiophene HDS reaction depends on the montmorillonite presence, zeolite Si/Al ratio (17,30,45) and the noble metal precursor. At the same Pt loading (1 wt.%), the total thiophene conversion over Pt(Cl)ZM catalysts was 33–40%, while the rate increased slightly with decreasing the zeolite Si/Al ratio from 45 to 17. The C_4-hydrocarbon formation rate was twice higher for 1Pt(Cl)ZM-17 than for 1Pt(Cl)ZM-30. At the same zeolite Si/Al ratio (e.g. Si/Al-45), doubling of the Pt loading increased the total thiophene conversion by 10% and reduced the rate by a factor of 1.4. At nearly the same Pt loadings (1.6 and 1.8 wt.%), the impregnated Pt-zeolite catalyst was 1.2 times more active in thiophene HDS than the ion-exchanged Pt-zeolite catalyst. Meanwhile, the ion-exchanged Pt-zeolite prepared by using tetraammineplatinum chloride showed higher selectivity to C_4-hydrocarbons in comparison with the impregnated Pt catalyst prepared from hexachloroplatinum acid. The regularities observed of thiophene HDS activity versus Pt-catalyst composition correlate with changes in the state of Pt and size of its particles.

The thiophene HDS activity of Pt catalysts supported on zeolite and on montmorillonite is also reported in Table 2. At the same Pt loading (1 wt.%) and Pt precursor, the Pt catalyst on the zeolite-montmorillonite monolith (e.g. Pt(Cl)ZM-45) was slightly more active and selective to C_4-hydrocarbons than the one on the zeolite (e.g. Pt(Cl)Z-45). Meanwhile, the Pt-montmorillonite catalyst (see Pt(Cl)M and Pt(A)M) was not selective to C_4-hydrocarbons, especially the 1Pt(Cl)M catalyst prepared by impregnation with hexachloroplatinum acid. The 1Pt(Cl)M catalyst had the highest activity in the thiophene hydrogenation to tetrahydrothiophene. This indicates that the zeolite channels play an important role in the sulphur removal from thiophene. On the other hand, the replacement of montmorillonite for alumina in the composition of the support decreased the activity by a factor of three, whereas the selectivity of thiophene decomposition did not change (see samples 2Pt(Cl)ZM-45 and 2Pt(Cl)ZA-45). When Pt was supported on monoliths containing Y-zeolite, silica or alumina with montmorillonite, we also observed low activity in thiophene decomposition (X_{C4H4S}-16–22%) and selectivity to C_4-hydrocarbons 47–54%, e.g. for 1Pt(Cl)YM, 1Pt(Cl)SiM, 1Pt(Cl)AlM. This indicates that both the textural properties and the proton acidity of the support play an important role in the thiophene hydrodesulphurization. The aggregate of these properties was more optimal when the monoliths were prepared from H-ZSM-5 with montmorillonite.

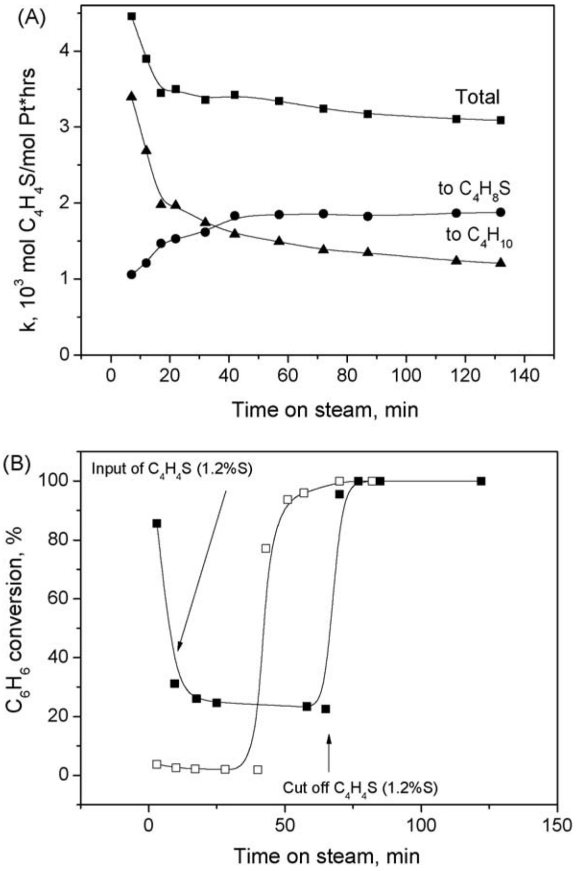

Fig. 7. (A) The rate of thiophene conversion by HDS and HYD routes versus duration time. The catalyst is 1Pt(Cl)ZM-45. (B) The benzene conversion on 1Pt(Cl)ZM-45 (■) and Pt/SiO_2 (□) versus duration time.

The most active catalyst 1Pt(Cl)ZM-45 was tested in benzene hydrogenation and hydrodesulphurization of diesel fractions.

Pt-zeolite catalysts have higher hydrogenation activity, e.g. in benzene hydrogenation, and stability to thiophene deactivation. Their benzene HYD activity was shown to be determined by the catalyst composition and the support acidity, as discussed above for thiophene desulphurization. Benzene conversion at 300 °C is close to 100% on our Pt-zeolite catalyst. If thiophene is introduced into the gas mixture at 300 °C, the benzene conversion decreases rapidly and reaches a stable value of 23–26%, whereas the thiophene conversion is 100% (Fig. 7B). MCP formation was observed on Pt(Cl)ZM-45 catalysts supported on zeolite-monoliths, and was not detected on commercially available Pt/SiO_2 (Pt ~ 0.5 wt.%). Benzene conversion to MCP was 5–8%. When the thiophene feeding was cut off, the benzene conversion sharply increased and reached 100% on the Pt-catalyst (Fig. 7B). The zeolite Si/Al ratio did not influence catalytic activity in benzene HYD of Pt-catalysts. It was noted that the 1Pt(Cl)ZM-45 catalyst possessed higher stability to deactivation by thiophene in comparison with commercially available Pt/SiO_2 (Fig. 7B). The benzene hydrogenation activity in thiophene presence over our Pt-zeolites was well correlated with tetralin hydrogenation activity observed for Pt-Pd/Y zeolite [36] and Pt-Pd/ASA [27,81] in presence of dibenzothiophene.

The performance of Pt supported on the zeolite-monolith in desulphurization and hydrogenation of Desulphurized Light Cycle Oil was evaluated on the IFP hydrotreating pilot plant. Table 3 presents the aromatic contents, the cetane numbers, the hydrogen contents and the sulphur contents measured in the products for stabilized chemical conditions. Figs. 8 and 9 show the density evolution versus time on stream and the distillation curves of the products for the three hydrogenation experiments on 1Pt(Cl)ZM-45 catalyst, respectively. The density of the liquid product obtained during the hydrogenation of DLCO on 1Pt(Cl)ZM-45 catalyst at 300 °C was observed to increase during the first 100 h. Then, the density reached a steady value (Fig. 8), which was lower than the one of the initial feed (Table 3). The smaller densities observed with the 1Pt(Cl)ZM-45 catalyst indicate higher hydrocracking activity of this catalyst. Indeed, the distillation curves of the products for the 1Pt(Cl)ZM-45 catalyst are different from those of the DLCO feed. The yield on liquid product (with distillation temperature above 100 °C) obtained on 1Pt(Cl)ZM-45 catalyst was close to 88% (Fig. 9). The crushed catalyst had higher hydrogenation activity than the monolithic catalyst. Their rate constants were 0.29–0.32 and 0.17–0.18 h^{-1}, respectively. The hydrogenation activity of the crushed catalyst increased twice when the sulphur content in the feed was decreased from 50 to 20 ppm. The differences observed in the performance of the crushed and the monolithic catalysts suggest intragranular diffusion limits on the monolith catalyst (in connection with the used loading). The slight decreasing of cetane numbers and the slight increasing of hydrogen contents obtained with the 1Pt(Cl)ZM-45 catalyst are also in accordance with its lower efficiency in hydrogenation in the presence of sulphur.

The test showed that 1Pt(Cl)ZM-45 catalyst had high activity in desulphurization of DLCO feeds containing 20–50 ppm of sulphur in the form of dibenzothiophene. At pressure 6 MPa and temperature 300 °C, the crushed and the monolithic catalysts decreased the sulphur concentrations to 0 and 2–3 ppm, respectively.

Our results show that both crushed and monolithic samples of the 1Pt(Cl)ZM-45 have rather high activity in desulphurization of the DLCO feeds, in hydrocracking it has moderate activity, and it is least active in hydrogenation.

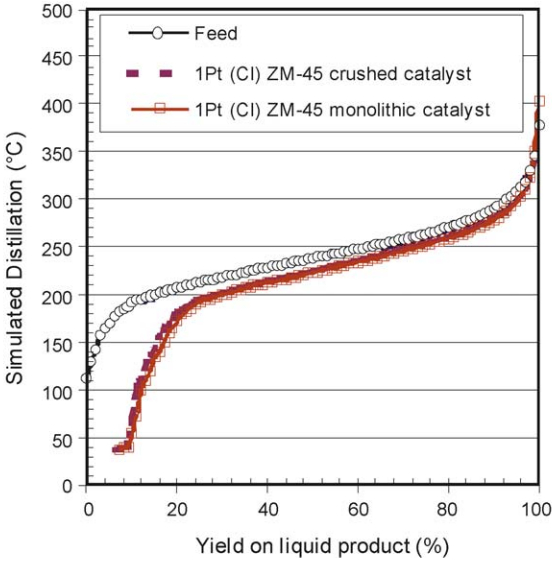

Fig. 9. Product distillation curve-comparison with the DLCO feed (reaction conditions: 50 ppm S (from DBT) in the feed).

4. Discussion

4.1. Electronic state of Pt

HRTEM, FTIR, XPS and EXAFS data correlate well with each other. According to TEM, the catalysts with any zeolite Si/Al ratio contain finely dispersed platinum species with size 2–5 nm located on the surface of the zeolite crystallites and montmorillonite. The ion-exchanged Pt-catalysts have also the well crystallized Pt^0 particles with prismatic shape and prevalent size 10–25 nm, which are located on the outside surface of the zeolite crystals. The main Pt-species state observed by FTIR of adsorbed CO molecules is Pt^0 (ν_{CO} = 2070–2095 cm^{-1}). Besides, the oxidized Pt^+/Pt^{2+} on surface of Pt^0-nanoparticles or close to cation-exchange zeolite site (ν_{CO} = 2122–2128 cm^{-1}), $Pt^{\delta+}$ in $PtO_{1-x}Cl_x$ particles (ν_{CO} = 2134–2138 cm^{-1}), Pt^{2+} (ν_{CO} = 2150–2155 cm^{-1}) and Pt^{3+} (ν_{CO} = 2196 cm^{-1}) are also presented. The electronic properties of the surface Pt atoms depend on their interaction with the support [57,59,61–63], and therefore on the preparation route of the Pt catalysts and the acidic properties of the supports.

According to the XPS and EXAFS data, the stabilization of the oxidized $Pt^{\delta+}$-state, indicated by BE of Pt $4f_{7/2}$ 72.5 eV and

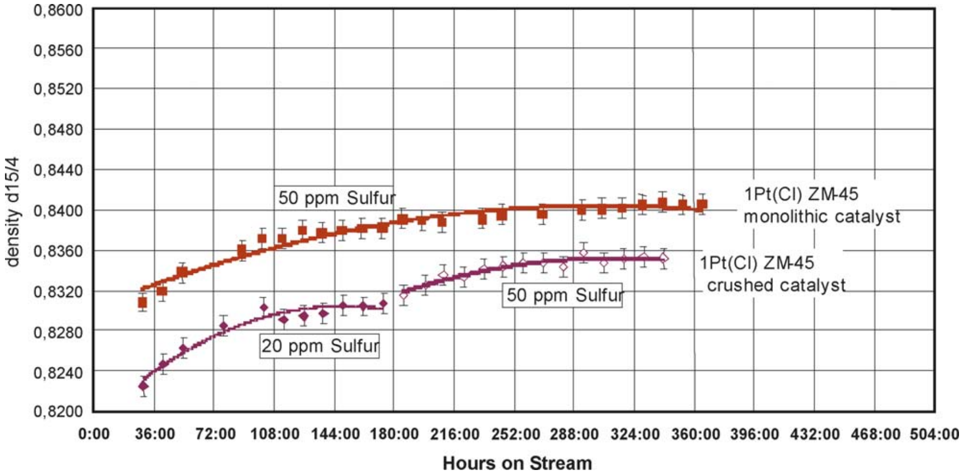

Fig. 8. Density evolution versus hours on stream.

R_{Pt-O} = 1.98A, R_{Pt-Cl} = 2.1A, is promoted by Ca-montmorillonite and hexachloroplatinum acid used as the Pt precursor. The oxidized $Pt^{\delta+}$-state can correspond to oxygenated and/or chloride platinum compounds with (Cl + O)/Pt ratio less than 2 (probably, $Pt(OH)_2$ or [Pt(OH)Cl] or [PtO_xCl_y]). The other oxidized $Pt^{\delta+}$-state can be assigned to metal species dispersed at atomic scale with the size smaller than 1 nm, having the strong interaction with the support. We do not exclude a possibility of Pt particles with size up to 1 nm being located inside the zeolite channels. In this case they are not visible by TEM. According to the data published in [51,52], the maximum size of Pt particles located inside the channels of the ZSM-5 zeolite is around 3.5 nm. The a.b. at 2090–2095 cm^{-1} in the FTIR spectra of adsorbed CO molecules could indicate the formation of small Pt particles located inside the zeolite channel close to the acid site. This hypothesis is also confirmed by the decrease of the acidic strength of Pt-zeolite in comparison with the H-zeolite, observed before for Pt-mordenite [64] and Pt-ZSM-5 [61]. In our case, the decrease of the acidic strength of Pt-zeolite is most significant when Ca-montmorillonite is added to the zeolite supports. The interaction of the electron-deficient Pt atoms or smaller Pt particles with one or two acidic hydroxyl groups located inside the zeolite channels can change the electron density in the conjugated base-acid, and therefore decrease the acid strength [61,64]. Similar interaction of large Pt particles located usually on outside surface should not affect the support acidity [64].

The formation of metal species dispersed at atomic scale is possible both for the ion-exchange and the impregnation preparation routes of Pt catalysts. The formation of such dispersed metal species can result from the ligand-exchange of Al-OH surface groups with hexachloroplatinic acid solution [59,67–69]. The ligand-exchange is well known to take place upon impregnating the alumina surfaces with hexachloroplatinic acid solution [68,69]. As a result, some of the Al-OH surface groups can be replaced by $[PtCl_6]^{2-}$ complexes with the formation of $[(AlOH)_2PtCl_4]$ and $[(AlCl)_2PtCl_4]$ surface complexes [67,68]. Such chlorines coordinating the Pt ions will prevent the Pt species from migrating during drying and calcinations. Most likely, some traces of chlorine are preserved on the catalyst surface after calcination and reduction with hydrogen [69]. The formation of $[Pt^{IV}(OH)_xCl_y]$ and $[Pt^{IV}O_xCl_y]$ was earlier found during calcinations at 300 °C and 500 °C, respectively, for Pt/Al_2O_3 catalyst prepared by impregnation with H_2PtCl_6 solution [74]. We assume that the Cl^- ions hinder $Pt^{+\delta}$ species from agglomeration and further reduction to Pt metal. This assumption correlates with a narrow size distribution of TEM-visible Pt particles for the catalyst prepared by incipient wetness impregnation with hexachloroplatinum acid. Our assumption agrees with previous investigations of supported Pt/Al_2O_3 catalysts [72–74]. These works have pointed out that chlorine is strongly bonded to the alumina and, then, the platinum oxide crystallites interact with it to form oxychloroplatinum complexes such as PtO_xCl_y up to 500 °C [72–74].

The formation of Pt metal (with BE of Pt $4f_{7/2}$ 71.1 eV and R_{Pt-Pt} = 2.75A) and hydroxy- or oxy-complex such as $Pt(OH)_6^{2-}$ or PtO_2 (with BE of Pt $4f_{7/2}$ 75.1 eV and R_{Pt-O} = 2.00 A) is observed when H-ZSM-5 powder or tetraammineplatinum chloride $Pt(NH_3)_4Cl_2$ is used for preparation of Pt catalysts. This assumption agrees with the FTIR data of adsorbed CO, because the absorption band at 2090 cm^{-1} typical of Pt^0 clusters and high frequency absorption bands at 2122, 2150, and 2196 cm^{-1} corresponding to the oxidized Pt species were observed for the ion-exchanged Pt samples. Observation of chlorine in survey XPS spectra (Cl2p line) of these samples, although its quantity was smaller than in impregnated catalysts, does not exclude the doping of Pt-species by Cl-ions. The formation of the positively charged Pt species (Pt^{2+}, a.b. 2155 cm^{-1} and Pt^{3+}, a.b. 2196 cm^{-1}) is possible as a result of the interaction of the $[Pt(NH_3)_4]^{2+}$ complex with the support via ion-exchange with the protons of bridged hydroxyls of the zeolite and montmorillonite. This interaction seems to be strong. So, the Pt complex remains on the surface during the drying process. During the calcination, the ammine groups decompose yielding Pt metal particles coordinated with the surface oxygen on the support [59,65–67]. Thus, calcination under mild conditions—the ambient air and temperatures up to 250 °C—will lead to evolution of ammonia which provides reducing media and formation of finely dispersed Pt^0 particles [65,66].

On the other hand, the formation of the large Pt metal particles is possible when the electrostatic interaction between the $[Pt(NH_3)_4]^{2+}$ complex and the support surface takes place. Above 250 °C in ambient air the NH_3 ligands are quickly oxidized with the formation of PtO particles [65,66]. When the temperature increases further, the small and mobile PtO particles merge leading to low metal dispersion. Besides, fast exothermic NH_3 oxidation may promote the particle sintering [66] and the formation of large Pt particles, which were observed by TEM. As mentioned above, the catalyst prepared by ion-exchange with $[Pt(NH_3)_4]Cl_2$ contains well-crystallized Pt^0 particles with prevalent size 10–25 nm. The large Pt^0 crystallites are located on the outside surface of the zeolite crystals.

The strong electronic interaction of Pt atoms or small Pt particles located inside the zeolite channels close to the zeolite proton sites changes significantly the electron density of both Pt and the zeolite, influencing the catalytic activity. The Pt-zeolite exhibits high catalytic activity in hydrogenation [27,36,59] and hydrogenolysis [10,27,78–80].

4.2. Catalytic activity

HDS reactions are generally performed at temperatures between 320 and 450 °C in the presence of hydrogen. Under these conditions, decomposition of thiophene usually leads to the formation of butadiene, *n*-butenes, and butane [71,72]. At 300 °C we observed also the formation of tetrahydrothiophene. The formation of C_4-hydrocarbons and tetrahydrothiophene suggests that there are two pathways of thiophene conversion: via direct hydrogenolysis of the C–S bond with the formation of intermediate butadienes (direct DDS pathway) and via prehydrogenation of the thiophene ring followed by the C–S bond breaking with formation of intermediate tetrahydrothiophene (HYD pathway). The relative contribution of each pathway is determined by the reaction conditions, by the type of substrate, and by the catalyst. However, thiophene, benzothiophene, dibenzothiophene and other reactive substances (mercaptans, sulphides, etc.) are known to react predominantly via the hydrogenolysis reaction pathway [10–13,21,22]. It is only in the case of 4- and/or 6-methyldibenzothiopene that the conversion following the DDS reaction pathway is significantly slowed down. So, they are removed via preliminary hydrogenation of one aromatic ring followed by expulsion of the sulphur atom [11–13].

As mentioned above, the selectivity to tetrahydrothiophene on our Pt-zeolite catalysts, e.g. Pt(Cl)ZM-45, does not decrease with time. This indicates that tetrahydrothiophene is a stable intermediate and sulphur removal from the fully hydrogenated sulphur-containing intermediate is unfavourable over the Pt-zeolite. The thiophene hydrogenation is the main pathway for thiopene decomposition on Pt-montmorillonite, e.g. Pt(Cl)M. It can be assumed that the tetrahydrothiophene formation takes place on the surface Bronsted acid site, and the zeolite channel plays an important role in its further transformations. The large kinetic diameter of tetrahydrothiophene and/or its strong interaction with the Bronsted acid site prohibit later tetrahydrothiophene penetration into the zeolite channels, where it would undergo rupture of the C–S bond. Meanwhile, a linear intermediate, such as S=C=CH–

CH=CH$_2$, which is formed as a product of thiophene decomposition via hydrogenolysis of the C–S bond, easily penetrates into zeolite channel, where it undergoes hydrogenation to C$_4$-products and H$_2$S [79].

At similar platinum loadings the activity and selectivity of Pt catalysts in thiophene HDS substantially depend on the method used for platinum deposition in the catalyst. At similar Pt loading (1 wt.%) the thiophene HDS activity of our Pt-zeolite catalyst increases with decreasing Si/Al ratio (from 45 down to 17), and when hexachloroplatinum acid is used as the precursor. However, the Pt-zeolite catalysts are more selective to C$_4$-hydrocarbon formation during thiophene removal, when tetraammineplatinum chloride and Ca-montmorillonite are used for the catalyst preparation.

The analysis of activity in thiophene HDS and other studied hydrotreating reactions as a function of catalyst composition shows their good correlation both with the support acidity and with the electronic states of platinum and its location. The Pt-zeolite catalyst containing the small Pt metal particles (1–5 nm) and the positively charged metal particles exhibit higher catalytic activity in thiophene hydrogenolysis and hydrocarbon hydrocracking. Our data agree with high activity in hydrogenation and isomerization of hydrocarbon observed for the catalyst containing well-crystallized Pt metal particles on the surface [59]. The strength and concentration of Bronsted acid sites affect the HDS activity of the catalysts prepared by impregnation with hexachloroplatinum acid. However, the process selectivity is affected more by location of platinum metal particles in the vicinity of BAS, which is possible if the catalyst is synthesized by ion-exchange.

A similar tendency to the increase of thiophene HDS activity with the decrease of the SiO$_2$/Al$_2$O$_3$ ratio in HZSM-5 was earlier observed for Pt/HZSM-5 [79]. Similar tendencies were observed for hydrogenation and isomerization of hydrocarbons on Pt/zeolite [59]. The high activity of Pt/HZSM-5 catalysts was explained by possible spillover of atomic hydrogen, which hydrogenates the zeolite surface species formed by thiophene decomposition after decomposition of molecular hydrogen on the metal. It is known that the BAS concentration in H-ZSM-5 decreases when the SiO$_2$/Al$_2$O$_3$ ratio decreases but their strength grows. The Bronsted acid sites of HZSM-5 and Pt particle accounting for activation of thiophene and hydrogen, respectively, play an important role in the hydrodesulphurization of thiophene on Pt/HZSM-5 catalyst [5,79].

Thus, the design of our catalyst conforms to the concept suggested by Song [10,42]. The catalyst is bifunctional. The activation of hydrocarbons and hydrogen takes place over the proton sites of the support and platinum metal particles, respectively. The catalyst has two types of pores. The channels of the ZSM-5 zeolite with diameter 0.55 nm act as micropores inaccessible to large organic molecules. Independent of the method used for deposition of platinum, there are two types of active platinum particles. The sites of the first type are platinum metal particles with the size 2–25 nm located on the surface of the zeolite crystallites and montmorillonite. These sites are accessible to large organosulphur molecules and sensitive to deactivation with sulphur. Yet, they are active in hydrogenation of aromatic molecules. The platinum sites of the second type are located inside the zeolite channels and inaccessible to the organic molecules. These sites account for activation of hydrogen used for regeneration of the deactivated sites of the first type. The electronic state of Pt in the sites of the second type has not been determined unambiguously. Probably, these are small Pt^0 particles located close to Bronsted acid sites. Such location facilitates spillover of hydrogen from Pt to the reaction intermediate. The presence of a larger number of Pt particles in contact with Bronsted acid sites favours the thiophene decomposition.

5. Conclusion

The Pt-zeolites are very active catalysts for thiophene hydrodesulphurization and benzene hydrogenation with high sulphur tolerance. The Pt-zeolite catalyst demonstrated high efficiency in ultra-deep desulphurization of DLCO. The good catalyst performance can be explained by the favourable pore space architecture and the location and the state of the Pt clusters. The catalyst has two types of well connected pores (micro and meso, macro) and contains two types of Pt particles—finely dispersed Pt nanoparticles (2–5 nm) and well-crystallized Pt^0 particles (10–25 nm)—located on montmorillonite and zeolite surfaces. The Pt-states are Pt^0 (ν_{CO} = 2070–2095 cm^{-1}) and oxidized Pt-species such as Pt$^{\delta+}$ (ν_{CO} = 2128 cm^{-1}) and Pt^{2+} (ν_{CO} = 2149–2155 cm^{-1}). The presence of Pt metal particles dispersed at atomic scale with the size smaller than 1 nm and located close to Bronsted acid sites in microporous zeolite channels has also been proposed based on the FTIR data.

Acknowledgments

This research was supported by INTAS (00-413), RFBR (06-03-33005a), RFBR (08-03-01150a), RFBR (08-03-90435-Ukr_a) and RAS Presidium (1.3) grants.

References

[1] European Directive for emissions of light duty vehicles (70/220/CE amended by 99/69/EC as Euro3 and 2002/80/EC as Euro4), European Directive for emissions of heavy duty vehicles (88/77/CE amended by 1999/96/CE as Euro4 and Euro5).
[2] Directive of the European Parliament and of the Council, Brussels COM (11.05.2001) 241 final (BS EN 590-2004/DIN EN 590-2004) Automotive fuels, Diesel, Requirements and test methods; and 2003/17/EC OJ L 76, 22.3.2003, p. 10.
[3] EPA-Diesel RIA, United States Environmental Protection Agency, Air and Radiation, EPA 420-R-00-026, December 2000; and Clean Air Act Tier 2; 1999.
[4] H. Topsoe, B.S. Glausen, F.E. Massoth, Hydrotreating Catalysis: Science and Technology, Springer-Verlag, Berlin, 1996, p. 310.
[5] E. Lecrenay, K. Sakanishi, I. Mochida, Catal. Today 39 (1997) 13.
[6] H. Topsøe, B. Hinnemann, J.K. Nørskov, J.V. Lauritsen, F. Besenbacher, P.L. Hansen, G. Hytoft, R.G. Egeberg, K.G. Knudsen, Catal. Today 107–108 (2005) 12.
[7] T. Kabe, A. Ishiharam, H. Tajima, Ind. Eng. Chem. Res. 31 (1992) 1577.
[8] X. Ma, K. Sakanishi, I. Mochida, Ind. Eng. Chem. Res. 33 (1994) 218.
[9] R. Shafi, G.J. Hutchings, Catal. Today 59 (2000) 423.
[10] C. Song, Catal. Today 86 (1–4) (2003) 211.
[11] I.V. Babich, J.A. Moulijn, Fuel 82 (2003) 607.
[12] M. Breysse, G. Djega-Mariadassou, S. Pessayre, C. Geantet, M. Vrinat, G. Perot, M. Lemaire, Catal. Today 84 (3–4) (2003) 129.
[13] S.K. Bej, S.K. Maity, U.T. Turaga, Energy & Fuels 18 (5) (2004) 1227.
[14] T.C. Ho, Catal. Today 98 (2004) 3.
[15] T. Fujihawa, M. Kato, H. Kimura, K. Kiriyama, M. Hashimoto, N. Nakajima, J. Jpn. Petrol. Inst 48 (2) (2005) 106.
[16] T. Fujihawa, M. Kato, T. Ebihara, K. Hagiwara, T. Kubota, Y. Okamoto, J. Jpn. Petrol. Inst 48 (2) (2005) 114.
[17] H.R. Reinhoundt, R. Troost, S. van Schalkwijk, A.D. van Langeveld, S.T. Sie, J.A.R. van Veen, J.A. Moulijn, Fuel Process. Technol. 61 (1999) 117.
[18] C. Song, K.M. Reddy, Appl. Catal. A 176 (1999) 1.
[19] G.R. Li, W. Li, M.H. Zhang, K.Y. Tao, Appl. Catal. A 273 (1–2) (2004) 233.
[20] J. Ramirez, G. Macias, L. Cedeno, A. Gutierrez-Alejandre, R. Cuevas, P. Castillo, Catal. Today 98 (1–2) (2004) 19.
[21] G. Perot, Catal. Today 86 (1–4) (2003) 111.
[22] C.E. Hedoire, C. Louis, A. Davidson, M. Breysse, F. Mauge, M. Vrinat, J. Catal. 220 (2) (2003) 433.
[23] E.Y. Kaneko, S.H. Pulcinelli, V. Teixeira da Silva, C.V. Santilli, Appl. Catal. 235 (2002) 71.
[24] L.J. Simon, J.G. van Ommen, A. Jentys, J.A. Lercher, Catal. Today 73 (2002) 105.
[25] H.R. Reinhoudt, R. Troost, A.D. van Langeveld, S.T. Sie, J.A.R. Van Veen, J.A. Moulijn, Fuel Process. Technol. 61 (1999) 133.
[26] H.R. Reinhoudt, PhD Thesis, Delft University of Technology, 1999, p. 225.
[27] R.M. Navarro, B. Pawelec, R. Mariscal, J.L.G. Fierro, J. Catal. 189 (2000) 184.
[28] S. Haji, Y. Zhang, D.F. Kang, M. Aindow, C. Erkey, Catal. Today 99 (2005) 365.
[29] A. Niquille-Rothlisberger, R. Prins, J. Catal. 242 (2006) 207.
[30] E. Furimsky, Appl. Catal. A 240 (2003) 1.
[31] P. Costa, J.-M. Manoli, C. Potvin, G. Djega-Mariadassou, Catal. Today 107–108 (2005) 520.
[32] P. Costa, C. Potvin, J.-M. Manoli, G. Djega-Mariadassou, B. Genin, Fuel 83 (2004) 1717.
[33] S.T. Oyama, J. Catal. 216 (2003) 343.
[34] M. Nagai, T. Fukiage, S. Kurata, Catal. Today 106 (2005) 201.
[35] C.S. Song, A.D. Schmitz, Energy & Fuels 11 (1997) 656.

[36] H. Yasuda, Y. Yoshimura, Catal. Lett. 46 (1997) 43.
[37] W. Qian, Y. Yoda, Y. Hirai, A. Ishihara, T. Kabe, Appl. Catal. A 184 (1999) 91.
[38] J.L. Rousset, L. Stievano, F. Aires, C. Geantet, A.J. Renouprez, M. Pellarin, J. Catal. 202 (2001) 163.
[39] T.B. Lin, C.A. Jan, J.R. Chang, Ind. Eng. Chem. Res. 34 (1995) 4284.
[40] H.R. Reinhoudt, R. Troost, S. van Schalkwijk, A.D. van Langeveld, S.T. Sie, H. Schulz, D. Chadwick, J. Cambra, V.H.J. de Beer, J.A.R. van Veen, J.L.G. Fierro, J.A. Moulijn, Stud. Surf. Sci. Catal. 106 (1997) 237.
[41] A. Ishihara, F. Dumeignil, J. Lee, K. Mitsuhashi, E.W. Qian, T. Kabe, Appl. Catal. A 289 (2005) 163.
[42] C. Song, Shape-selective catalysis, chemicals synthesis and hydrocarbon processing, in: ACS Symposium Series 738, Washington, (1999), p. 381;
C. Song, Chemtech 29 (3) (1999) 26.
[43] C. Song, X. Ma, Appl. Catal. B: Environ. 41 (2003) 207.
[44] S.A. Yashnik, Z.R. Ismagilov, A.N. Startsev, V.P. Doronin, I.V. Babich, J.A. Moulijn, Sulphur-resistant Catalysts for Hydrodesulphurization and Hydrogenation of Motor Fuels, Russian Application No. 2296618, priority from August 8, 2005, published 10.04.2007.
[45] R.V. Zagrafskaja, A.P. Karnaukhov, V.B. Fenelonov, Kinet. Catal. 20 (2) (1979) 465.
[46] E.A. Paukshtis, Infrared Spectroscopy in Heterogeneous Acid-Base Catalysis, Nauka, Novosibirsk, 1992 (in Russian).
[47] D.I. Kochubey, EXAFS Spectroscopy of Catalysts, Nauka, Novosibirsk, 1992 (in Russian).
[48] N. Binsted, J.V. Campbell, S.J. Gurman, P.C. Stephenson, SERC Daresbury Laboratory EXCURV92 program (1991).
[49] Yu.I. Yermakov, A.N. Startsev, V.A. Burmistrov, Appl. Catal. 11 (1984) 1.
[50] Z.R. Ismagilov, S.A. Yashnik, N.V. Shikina, et al. Book of Abstracts 13th Intern. Congress on Catalysis (ICC-13), 11-16 July, Paris (France), part 1, p. 108.
[51] P. Kubanek, H.-W. Schmidt, B. Spliethoff, F. Schuth, Micropor. Mesopor. Mater. 77 (2005) 89.
[52] D. Exner, N.H. Jaeger, A. Kleine, G. Schulz-Ekloff, J. Chem. Soc. Faraday Trans. I 84 (1988) 4097.
[53] A. Bourane, O. Dulaurent, D. Bianchi, J. Catal. 195 (2) (2000) 406.
[54] E. Rogemond, N. Essayem, R. Frety, V. Perrichon, M. Primet, M. Chevrier, C. Gauthier, F. Mathis, J. Catal. 186 (2) (1999) 414.
[55] P.J. Levy, V. Pitchon, V. Perrichon, M. Primet, M. Chevrier, C. Gauthier, J. Catal. 178 (1) (1998) 363.
[56] G.J. Arteaga, J.A. Anderson, C.H. Rochester, Catal. Lett. 58 (4) (1999) 189.
[57] K. Chakarova, M. Mihaylov, K. Hadjiivanov, Micropor. Mesopor. Mater. 81 (2005) 305.
[58] K. Chakarova, M. Mihaylov, K. Hadjiivanov, Catal. Comm. 6 (2005) 466.
[59] J.I. Villegas, D. Kubicka, H. Karhu, H. Osterholm, N. Kumar, T. Salmi, D.Yu. Murzin, J. Mol. Catal. A: Chem. 264 (2007) 192.
[60] S. Ito, H. Tanaka, Y. Minemura, S. Kameoka, K. Tomishige, K. Kunimori, Appl. Catal. A: Gen. 273 (2004) 295.
[61] A. Stakheev, E. Shpiro, O. Tkachenko, N. Jaeger, G. Schulzp-Ekloff, J. Catal. 169 (1997) 382.
[62] A. Solomennikov, A. Davydov, Kinet. Catal. 25 (1984) 403.
[63] Y. Yamasaki, M. Matsuoka, M. Anpo, Catal. Lett. 91 (2003) 111.
[64] V.L. Zholobenko, G.-D. Lei, B.T. Carvill, B.A. Lerner, W.M.H. Sachtler, J. Chem. Soc. Faraday Trans. 90 (1994) 233.
[65] A. Munoz-Paez, D.C. Koningsberger, J. Phys. Chem. 99 (12) (1995) 4193.
[66] A. Goguet, D. Schweich, J.-P. Candy, J. Catal. 220 (2003) 280.
[67] J. Dawody, M. Skoglundh, S. Wall, E. Fridell, J. Molec. Catal. A: Chem. 225 (2005) 259.
[68] B.N. Shelimov, J.-F. Lambert, M. Che, B. Didillon, J. Molec. Catal. A: Chem. 158 (1) (2000) 91.
[69] W.A. Spieker, J. Liu, J.T. Miller, A.J. Kropf, J.R. Regalbuto, Appl. Catal. A 232 (1–2) (2002) 219.
[70] C.D. Wagner, W.M. Riggs, L.E. Davis, J.F. Moulder, G.E. Muilenberg, Handbook of X-Ray Photoelectron Spectroscopy, Perkin-Elmer, Eden, Prairie, MN, 1979.
[71] A. Muiioz-Phezt, D.C. Koningsberger, J. Phys. Chem. 99 (1995) 4193.
[72] G.I. Straguzzi, H.R. Aduriz, C.E. Gigola, J. Catal. 66 (1980) 171.
[73] T.J. Lee, Y.G. Kimi, J. Catal. 90 (1984) 279.
[74] H. Lieske, G. Lietz, H. Spindler, J. Volteri, J. Catal. 81 (1983) 8.
[75] ICSD database, Collection codes: 22073, 2722, 2582, 44512, 65296.
[76] ICSD database, Collection codes: 15271, 8256, 26599, 202407, 24922, 24923.
[77] ICSD database, Collection code: 64923.
[78] M. Sugioka, F. Sado, Y. Matsumoto, N. Maesaki, Catal. Today 29 (1996) 255.
[79] M. Sugioka, F. Sado, T. Kurosaka, X. Wang, Catal. Today 45 (1998) 327.
[80] Y. Yoshimura, H. Yasuda, T. Sato, N. Kijima, T. Kameoka, Appl. Catal. 207 (2001) 303.
[81] R. Navarro, B. Pawelec, J.L.G. Fierro, P.T. Vasudevan, J.F. Cambra, P.L. Arias, Appl. Catal. A 137 (1996) 269.